Absolute Effective Areas of the HETGS

N.S. Schulz, S.C. Taylor, D. Dewey, H.L. Marshall

Center for Space Research, M.I.T., Cambridge, MA 02139

July 1999

ABSTRACT

Absolute effective area measurements of the flight-configuration Chandra High-Energy Transmission Grating Spectrometer (HETGS) were performed at the X-ray Calibration Facility (XRCF) during Phase H testing. The results of these measurements are compared with effective area predictions based on models of the individual HETGS components: the High Resolution Mirror Assembly (HRMA), the High-Energy Transmission Grating (HETG), and the AXAF CCD Imaging Spectrometer Spectroscopy array (ACIS-S).

The energy range from 0.48 to 8.7 keV was sampled at over 75 energies using x-rays produced by three of the sources available in the XRCF X-ray Source System (XSS). The Double Crystal Monochromator (DCM) provided dense coverage of the range 0.9 keV to 8.7 keV; the High Resolution Erect Field (grating) Spectrometer (HiREFS [reference: specifically HIREFS-SXR-1.75 grating monochromator from Hettrick Scientific Inc.]) provided data points in the 0.48 keV to 0.8 keV range; and x-ray lines from several targets of the Electron Impact Point Source (EIPS) covered the range from 0.525 keV (O-K) to 1.74 keV (Si-K).

The absolute effective area was measured as the ratio of the focal plane rate detected in a line to the line flux at the HRMA entrance aperture. A set of four Beam Normalization Detectors (BNDs) located around the HRMA were the prime source of flux determination. A variety of analysis techniques and considerations were applied including beam uniformity corrections, line deblending, and ACIS pileup. Uncertainties in the measurements are assigned based on counting statistics and estimates of analysis systematics; typically each measurement has an assigned error of order 10%.

The data indicate that we are very close to realizing our goal of a 10% absolute effective area calibration for the first-order effective area. The measurement-model residuals are seldom outside a $\pm 20\%$ range for both the High Energy Grating (HEG) and the Medium Energy Grating (MEG) first-order areas. Systematic variation of the residuals appear at a level of -10% in the energy range below 1.3 keV; in the 2.5 keV to 5 keV range a consistent +3% to +7% over prediction is seen. The regions of greater systematic variation, 1.3 to 2.5 keV and above 5 keV, are most likely dominated by uncompensated DCM beam uniformity effects and ACIS grade migration effects respectively.

Keywords: x-ray, diffraction, grating, calibration, CCD, monochromator, spectroscopy

1. INTRODUCTION

The HETGS on-board NASA's Chandra X-ray Observatory (formerly AXAF) is designed to perform high resolution x-ray spectroscopy with spectral resolving power of up to $E/dE \sim 1000$ in the 0.5 to 10 keV energy band. The HETGS results from the combined operation of the HRMA, the HETG which can be inserted into the optical path just behind the mirror assembly, and the ACIS-S located in the Chandra focal plane. As a backup configuration the spectrometer could also operate with the High Resolution Camera (HRC-I) in the focal plane. Detailed descriptions of the HETGS have been given in previous SPIE conference proceedings,[8,12,13] but we also want to encourage the interested reader to consult the AXAF Observatory Guide[17] for a general overview of Chandra and the HETG web site (see note below) for up-to-date information about the HETGS. The 1998 SPIE conference proceedings[14] contain a preliminary version of this report.

The central parts of the spectrometer are the two sets of transmission gratings, MEG facets of 4000 $\AA$ period and HEG (2000 $\AA$ period) facets, which together form the HETG. Figure 1 shows a photo of the HETG flight instrument.

Other author information: Send correspondence to N.S. Schulz.: Email: nss@space.mit.edu; Telephone: 617-258-5767; Fax: 617-253-8084

Up-to-date information available at: `http://space.mit.edu/HETG/`

It consists of four concentric rings tiled with grating facets, each ring intercepts the optical path of the corresponding type-I Wolter mirror pair of the HRMA in order to diffract the x-rays before they hit the focal plane. X-rays feeding the MEG come from the two outer HRMA shells, designated 1 and 3; these facets are optimized for efficiency in the lower part of the Chandra energy band. The HEG intercepts x-rays from the two inner shells, designated 4 and 6, and these facets are optimized towards the higher energies. The dispersion axes of MEG and HEG are offset by approximately 10 degrees, in order to fit the dispersed spectra from both grating types onto one detector array, minimizing any spatial interference between the two.

The HETG has been designed to place each facet at its prescribed location and orientation on a Rowland torus[12,13,15] with a diameter of 8635 mm. Therefore the "focal plane" of the spectrometer is actually not a plane but an approximation to a portion of the Rowland torus at 8635 mm distance. In order to match that Rowland torus in the focal plane, the detector consists of 6 imaging CCDs in a 1x6 array, which are tilted along the torus. An illustration of the focal plane view is shown in Figure 2 using a continuum measurement with the HETGS. For a detailed description of ACIS, see the 1998 SPIE paper[3] and ACIS Team Calibration Report.[4,5] This grating readout array, ACIS-S, consists of two different types of CCDs, 4 front illuminated devices (FI) and 2 back illuminated devices (BI), which are arranged in an array denoted by S0 to S5 (going from -Y to +Y in Chandra coordinates), in the illustration from left to right. S1 and S3 are the two BI devices. The position of the 0^{th} order image, which for HEG and MEG coincides with where the two dispersed continua cross each other (small black box), is on the back illuminated device S3. This will also be the launch-locked focal position for Chandra.

2. DEFINITIONS AND INPUT CALIBRATION PRODUCTS

The modeled HETGS effective area in general is calculated from 3 contributing elements, the HRMA single shell effective areas (A_s), the effective HETG grating efficiencies (G_s) for the mirror shells, and the ACIS-S photon detection efficiencies (QE_{ACIS}),

$$A_{HETGS}(E, m, mode) = \sum_{s=1,3,4,6} A_s(E)\ G_s(E, m)\ QE_{ACIS}(E, \vec{X}, mode). \quad (1)$$

Here E denotes the dependence on energy, m the diffraction order, *mode* the event identification in the CCD (here, for example, we will consistently use the sum of ASCA grades 0,2,3,4,6 and TE-mode), and the $\vec{X}$ dependences from spatial dependencies in the detector array, i.e FI/BI efficiencies and gap locations between the devices and position on the array.

The CXC calibration group has set up a repository for intermediate calibration products. The top level of this set of disk files is given here by the environment variable `CALDBaxafcal`. Under this top level directory, the files are organized by instrument, *e.g.* `$CALDBaxafcal/hetg`. References to specific files are given in the text of this document.

Figure 3 shows the Chandra HRMA on-axis effective area at XRCF for each shell (file: `$CALDBaxafcal/hrma/cip/hrmaD1996-11-01XeffareaN0004.rdb`). Mirror shells 1 and 3 cut off at energies around 5 and 6.5 keV, while shells 4 and 6 extend up to 7 and 9 keV. The decrease near 2 keV is due to the iridium M-edge in the reflective mirror coating.

Figure 4 shows the average quantum efficiencies for each ACIS-S detector array (files: `$CALDBaxafcal/acis/cip/acis*D1997-04-17qeobfN0002.dat`). The functions already include the transmission characteristics of the optical blocking filters. S1 and S3 are both back illuminated (BI) devices, while S0, S2, S4, and S5 are front illuminated (FI) devices.

An intrinsic spatial dependence of QE is apparent in BI devices, which suffer from large charge transfer inefficiency effects and the QE function is not a flat field across the device. This spatial variation has been included in computing model predictions. Here we used the 32x32 pixel QE maps provided by the MIT ACIS team and which are published in the ACIS calibration report to create a position dependent QE (directory: `$CALDBaxafcal/acis/cmp/bi_ratio_uni_N19980918/`). To do this we assumed a nominal position for the 0^{th} order of (x,y)=(4165,2215) in tiled detector coordinates and a defocus of 36 mm. Both of these assumptions were needed to compute the dispersion distance to energy conversion. The flat field maps were taken at 8 different energies (0.277, 0.525, 0.677, 1.74, 2.014, 4.511, 6.404, and 8.048 keV), and are averaged over 32x32 pixel regions. Instead of interpolating, the correction was made using the data from the nearest pixel and energy available. This results in some discontinuities in the QE curves, typically less than a few percent.

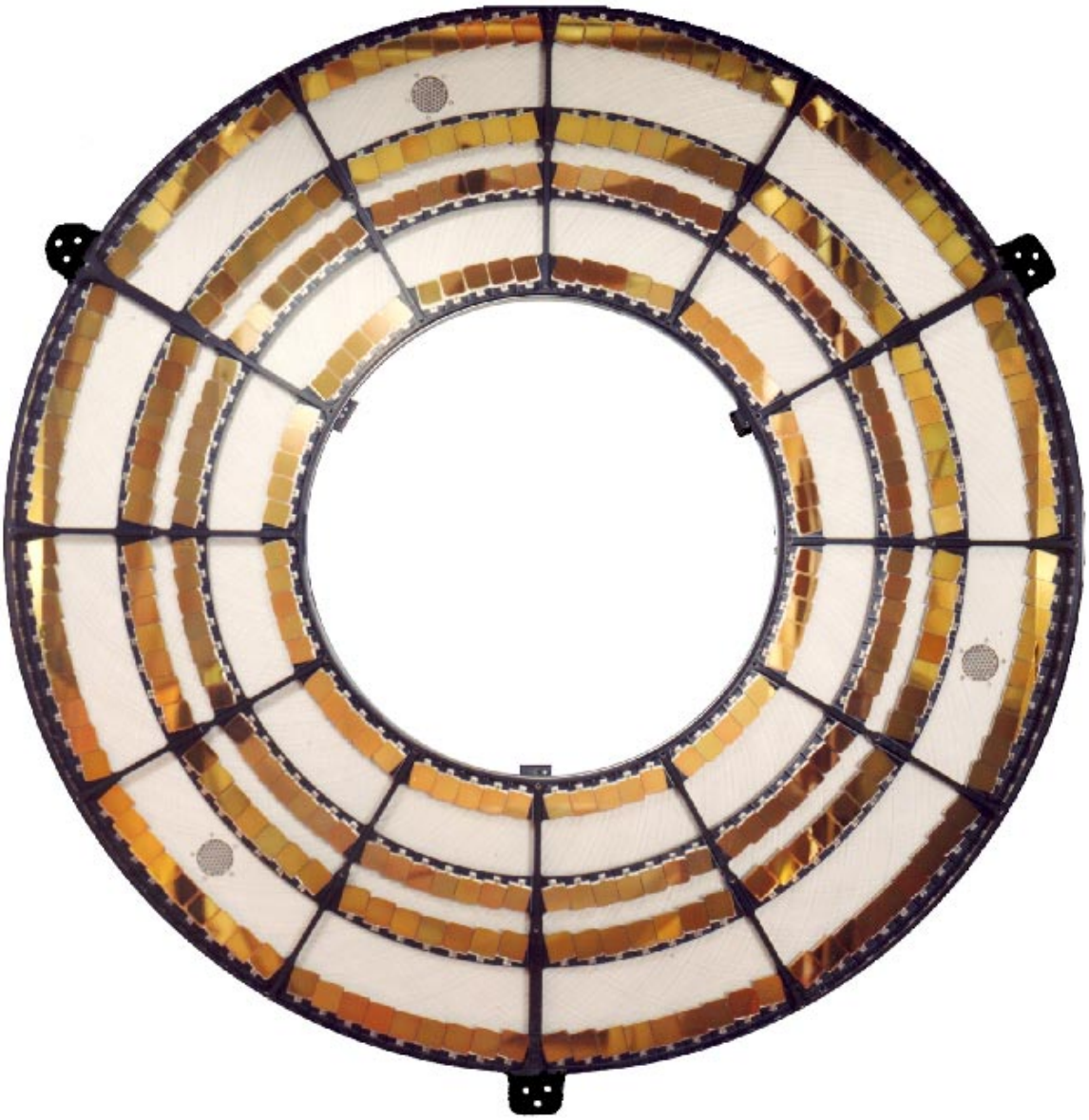

Figure 1. A photograph of the HETG assembly. It is made of 336 grating facets attached to a light-weight aluminum structure. The two outer rings are tiled with MEG facets, the two inner rings have HEG facets.

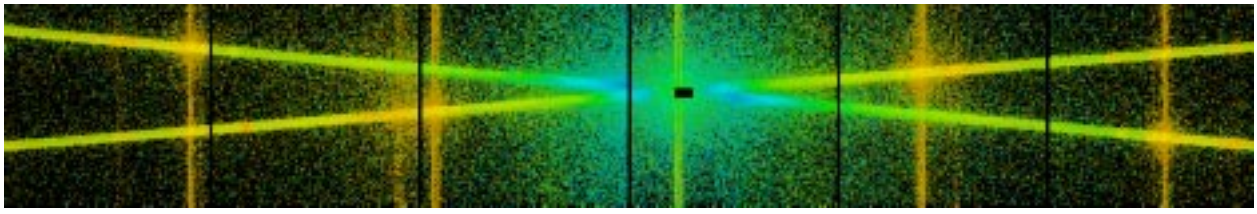

Figure 2. Continuum measurement using the HETGS at XRCF. An unfiltered Cu-anode source produces a broad-band x-ray continuum that is spread out along the HEG and MEG dispersion axes. The illustration shows the set-up of the six CCD devices (S0 to S5 from left to right, with the gaps between the devices. The MEG disperses into the upper right (and lower left corner), the HEG into the lower right (upper left corner). The vertical traces that appear at the 0^{th} order image as well as at Cu-L (0.93 keV) are CCD-frame transfer read-out effects.

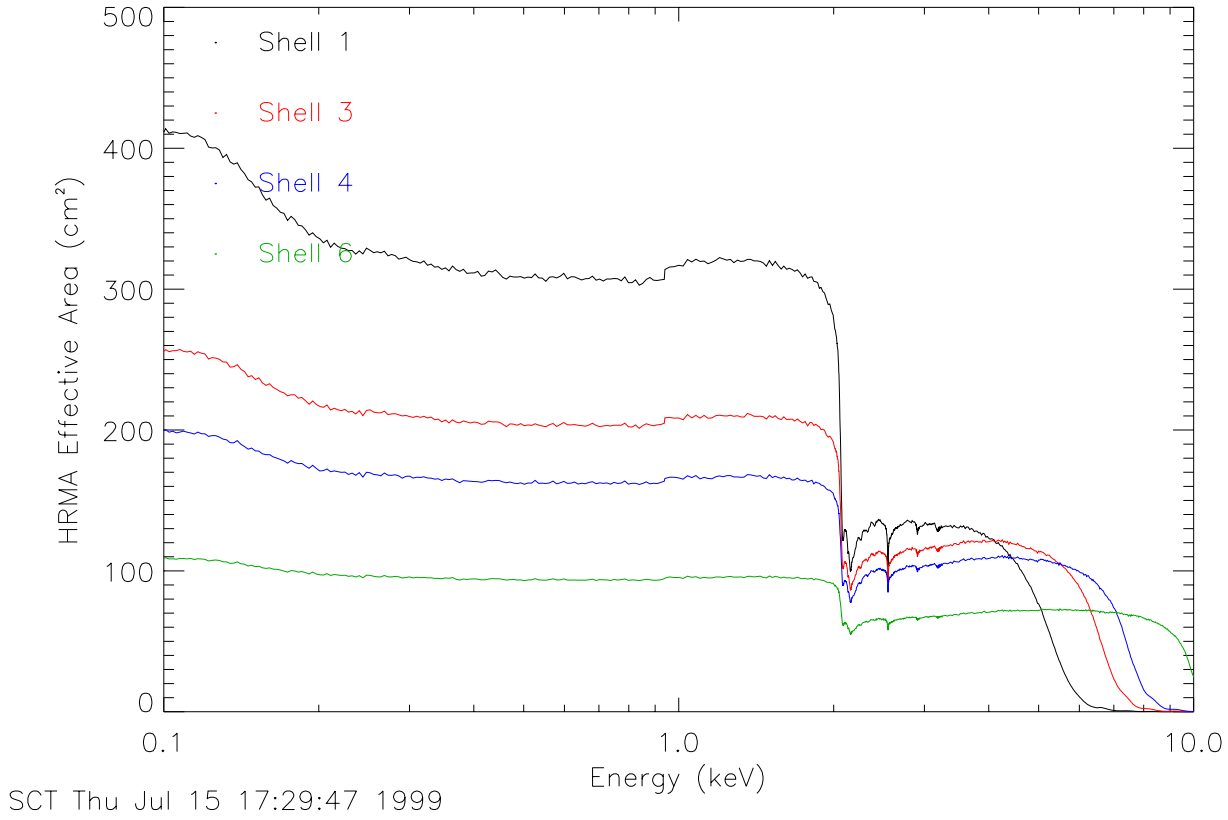

Figure 3. HRMA effective areas for each shell (courtesy of the Chandra Mission Support Team and Telescope Scientist Team, May, 1999). Shell 1 is shown in black, 3 in red, 4 in blue, and 6 in green.

The grating efficiencies have been determined at the X-ray Grating Evaluation Facility (X-GEF) at MIT.[7,9] The diffraction efficiency of each flight grating was measured at several energies, orders, and positions within each facet. Figure 5 shows the predicted effective efficiencies for MEG and HEG, see the memo:
`http://space.mit.edu/HETG/effic/effic.html`, and the data in
`$CALDBaxafcal/hetg/cip/hetgmegD1996-11-01greffN0002.rdb` and
`$CALDBaxafcal/hetg/cip/hetghegD1996-11-01greffN0002.rdb`. The effective area sum, Equation 1, then uses the MEG efficiency for s = 1 and 3 and the HEG efficiency for 4 and 6.

3. MEASUREMENTS AT XRCF

In April 1997 the HETGS underwent extensive testing at the X-Ray Calibration Facility (XRCF) at the Marshall Space Flight Center (MSFC).[19,20] The measurements designed for HETGS effective area calibration were performed using a variety of x-ray sources and detectors in order to cover the whole effective energy range with high resolution lines of sufficient power.[8] In this report we focus on measurements performed with the DCM, the EIPS, and the HiREFS covering a total energy range of 0.5 to 8.7 keV. During this phase "H" of XRCF testing, the ACIS-S array was the only detector in the focal plane. The setup also included several BNDs; here we make use of the four BNDs positioned at the HRMA entrance plane to estimate the incident flux.

3.1. DCM Measurements

3.1.1. Characteristics

The DCM is part of the XSS used at XRCF.[11,16] It offered three different crystals for these tests, of which we only used the Thallium Acid Phthalate (TAP) between 0.9 and 2.5 keV and the germanium (Ge111) between 2.5

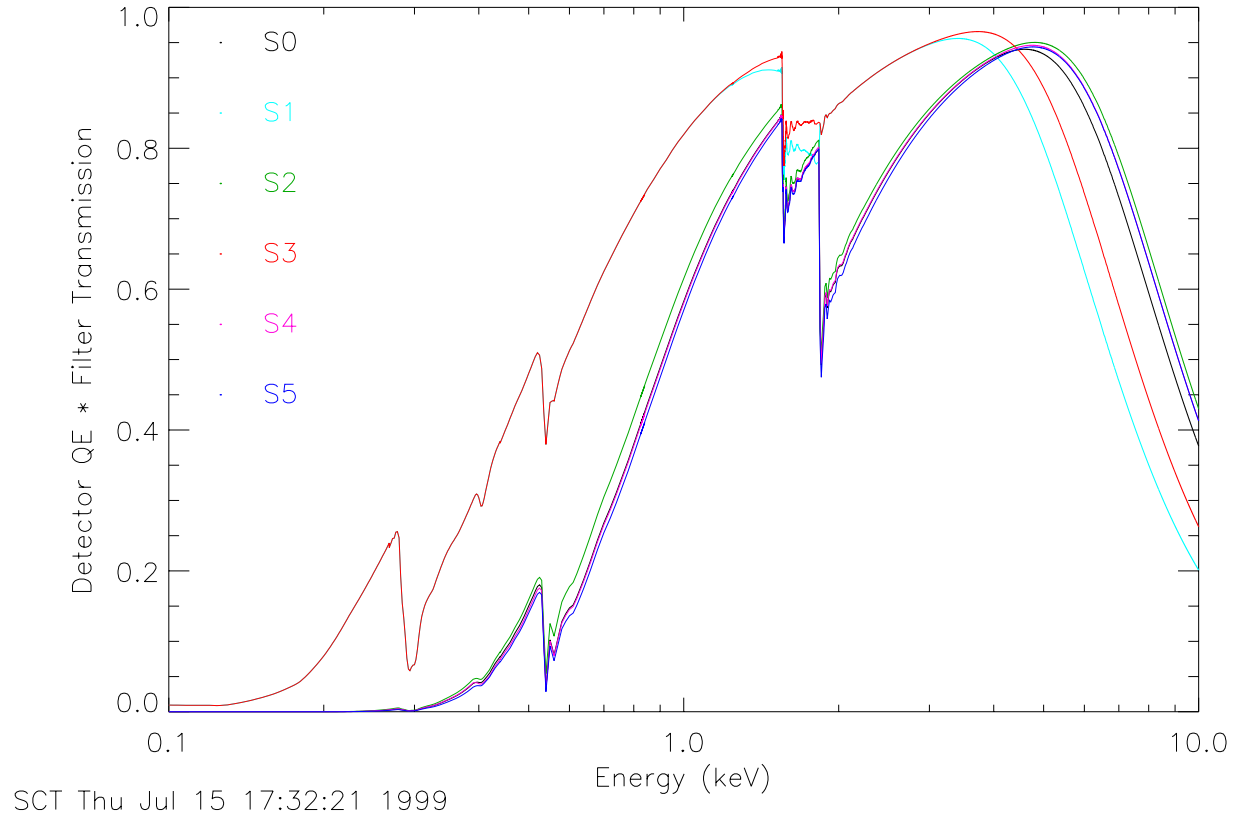

Figure 4. Effective efficiencies (quantum efficiency × filter transmission) as a function of energy for each of the ACIS-S detectors (courtesy of the MIT ACIS team, August 1998). The curve for chip S4 cannot be seen for most of the energy range, because it is very similar to the curve for chip S5. These curves represent the average QE over the entire array, and do not include variations in the QE over the array.

and 8.7 keV. The source is a rotating-anode tungsten source, which operates at a high voltage to generate a strong continuum, however it also produces several bright W lines at 1.38, 1.78, and 1.84 keV. Those lines actually proved quite useful for testing of HETG scattering.[6] The DCM has an energy gradient in the dispersion direction, which results in a non-negligible beam nonuniformity when tuned near the the W lines. Another source of nonuniformity is introduced while using the TAP crystal due to some waviness on the crystal's surface.

3.1.2. Energy Scans

The energy scans taken with the DCM include a total of 70 steps; Table 1 summarizes these measurements. The measurements were divided into 9 blocks with different increments. The first 2 blocks consisted of 8 steps of 50 eV starting from 950 eV, the next 3 blocks covered an energy range between 1.4 and and 2.4 keV in 30 eV steps, followed by 150 eV steps until 4 keV. The increments were then increased up to 500 eV until 8.7 keV.

In order to get sufficient photon counting statistics in the diffracted orders, the high voltage of the tungsten source was steadily increased above 2.5 keV. The total number of counts for each energy step then varied between 1.1×10^4 to 4.5×10^4 counts. Figure 6 shows a typical measurement, which included 11 steps between 2.5 and 4.0k eV. The detector was moved 20 mm out of focus along the optical axis towards the HRMA in order to spread the focal image over as many detector pixels as possible. The dispersed images appear as rings reflecting the two outer mirror shells in the MEG, the two inner shells (and therefore smaller rings) for the HEG. Each order appears as a sequence of rings separated by the dispersed increment of 150 eV.

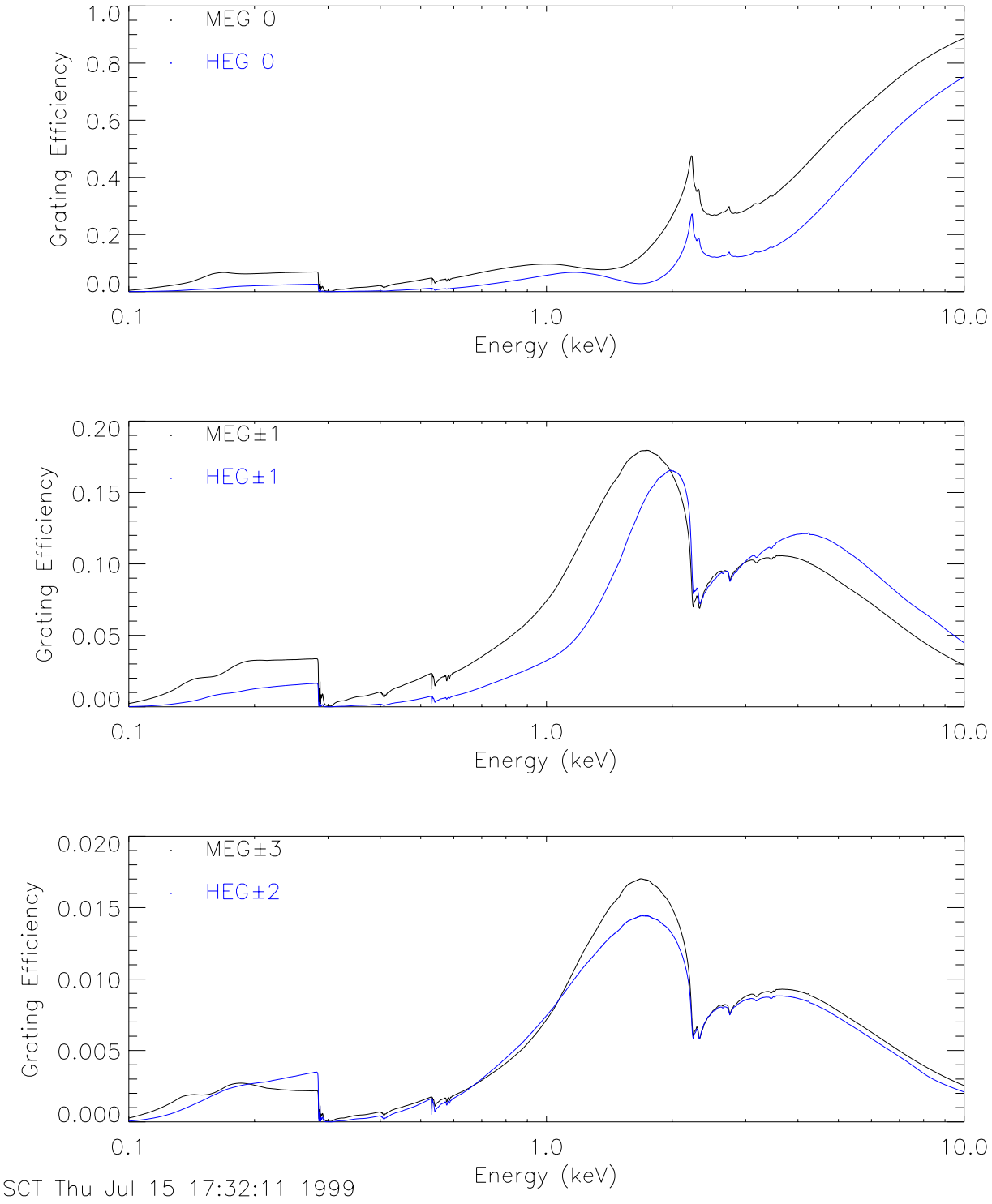

Figure 5. MEG and HEG modeled effective efficiencies as a function of energy. The top plot shows MEG and HEG 0^{th} orders, the middle, MEG and HEG $\pm 1^{st}$ orders, and the bottom, MEG $\pm 3^{rd}$ and HEG $\pm 2^{nd}$ orders. In each plot, MEG is shown in black and HEG is shown in blue.

TRW-ID H-HAS-EA-	DCM crystal	Energy eV	Increment eV	steps	∼counts/step	∼counts/s
8.001	TAP	950	50	5	41000	24.9
8.002		1200	50	5	45000	65.1
8.003		1400	30	11	28000	58.4
8.004		1860	20	8	35000	86.9
8.005		2050	30	11	12000	41.5
8.006	Ge1	2500	150	11	18000	50.0
8.007		4000	200	6	18000	60.5
8.008		5000	250	9	28000	60.9
8.009		7200	500	4	23000	33.0

Table 1. List of HETG effective area measurements with the DCM at XRCF. The energies listed are the start energies of each set. Exposure times varied between ∼1000 and 2000 s for each energy.

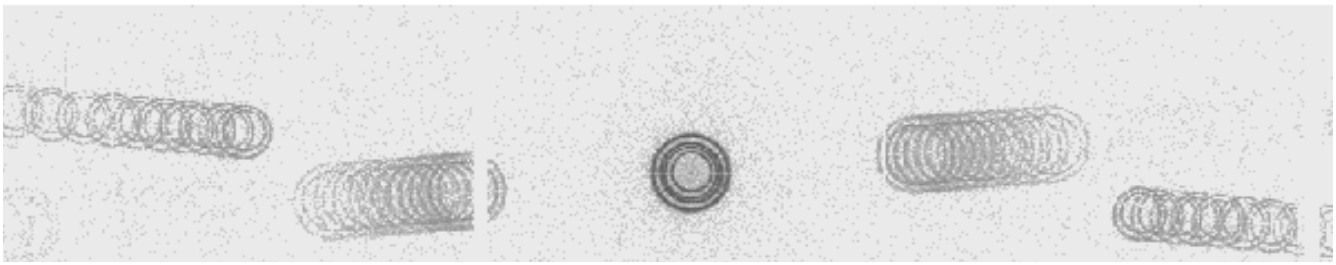

Figure 6. HETGS image of measurement H-HAS-EA-8.006. The image includes MEG and HEG 1^{st} order. Each order consists of 11 steps 150 eV apart.

3.2. EIPS Measurements

3.2.1. Characteristics

The EIPS is another part of the XSS used at XRCF,[11,16] where x-rays are produced by an electron beam incident on a target. The targets that were used for effective area analysis are O, Fe, Al, Si, and Cu anodes. The spectra generated by the EIPS do not suffer from the W contamination as apparent in the DCM measurements; however, EIPS are not entirely monochromatic and usually the target line sits on a strong continuum and is accompanied by other excitations from within the target material. Also there are fewer energies available. See `http://wwwastro.msfc.nasa.gov/xray/axafps_xss/peiscat.html` for further description of the Electron Impact Point Source, and the source spectra.

3.2.2. Source Energies

The experiments and sources that were used for this part of the effective area analysis are listed in Table 2, spanning an energy range of 0.525 to 8.048 keV. However, the two high energy line sources, Fe Kα and Cu Kα, were heavily piled-up and therefore excluded from further analysis. Also, the β lines for Al K and Si K and the η line for Fe L were weak enough to consider as part of the continuum for analysis purposes.

3.3. HiREFS Measurements

3.3.1. Characteristics

The HiREFS is a low energy monochromator x-ray source and, like the DCM, it also has a rotating anode source. Anodes of W and C were available, but only the data taken with the W anode were used for this analysis. It uses diffraction from a reflection grating for the energy selection. The benefit of the HiREFS is a tunable source with

TRW-ID H-HAS-EA-	Source	Primary Line	Energy eV	Other Lines or Contaminants	Average Count Rate /second
2.001	Al	Kα	1487	Al Kβ	85.7
6.001	O	Kα	525	-	20.8
6.002	Fe	Lα	705	Fe Lη, Fe Ll, O Kα	26.5
6.003	Cu	Lα	930	Cu Lζ	58.1
6.004	Si	Kα	1740	Si Kβ	89.1
6.005	Fe	Kα	6404	-	57.3
6.006	Cu	Kα	8048	-	59.6

Table 2. EIPS experiments used for effective area calculation. Throughout all measurements, the source rate stayed approximately constant. In the case of 6.002, the source was turned on at an average count rate of 17.7 c/s for 660 s, then turned off, and then turned back on to an average count rate of 33.4 c/s for 1200 s.

much lower available energies than the DCM. However a consequence of its reflection grating design is that the incident beam is not uniform, and the HiREFS spectrum contains substantial higher order lines, that is E_o, $2E_o$, $3E_o$, etc. This creates an "order overlap" problem when the HiREFS is combined with a grating spectrometer, such as HETGS, *e.g.* , the HiREFS 2^{nd} order, $2E_o$, when diffracted into the HETGS 2^{nd} order exactly overlaps spatially with the primary "1^{st} order 1^{st} order" image.

3.3.2. Energies

The experiments and sources that were used for this part of the effective area analysis are listed in Table 3. The lines selected for this analysis were 486 eV, 577 eV, 642 eV, 751 eV, 784 eV (2^{nd} order of the 392 eV line), 800 eV, and 972 eV (2^{nd} order of the 486 eV line). Above 1 keV, the data are contaminated by W lines, and were, therefore, excluded. The count rates shown in Table 3 are the total rates for all events.

TRW-ID H-HAS-EA-	Primary Energy(eV)	Other Energies (eV)	Average Count Rate /second
10.001	392	784, 1176, 1568	21.2
10.002	486	972, 1458, 1944	27.2
10.003	577	1154, 1731, 2308	31.5
10.004	642	1284, 1926, 2568	29.9
10.005	751	1502, 2253, 3004	28.3
10.006	800	1600, 2400, 3200	25.5

Table 3. HiREFS experiments used for effective area calculation. Throughout all measurements, the source rate stayed approximately constant. All available energies are listed, but the ones used for this analysis are underlined. For all cases, W lines at 1.38, 1.78, and 1.84 keV, were also visible.

4. DATA REDUCTION

The measured effective area of an HETG order is the ratio of the count rate of that particular order received by the CCD array to the incident source flux at the HRMA entrance plane.

$$A_{meas}(E, m, mode) = \frac{\text{focal plane counts/s in order}}{\text{source flux at HRMA}} [\frac{\text{counts/s}}{\text{photons/cm}^2\text{s}} = \text{cm}^2 \frac{\text{counts}}{\text{photon}}] \quad (2)$$

Therefore, in this report we are attempting to extract the count rate at the focal plane for a line in a given order, as well as determine the source flux of that line from the BND measurements.

4.1. Focal Plane Analysis

The event lists used for this analysis were provided by the ACIS team at Penn State University, who separated the telemetry data stream into the proper test segments and performed bias subtraction. Event grading and pulse height gain correction were performed here at the MIT Chandra X-ray Center (CXC). Since in this analysis we restrict the event selection to a standard grade set (ASCA grades 0,2,3,4,6), we additionally assign ASCA grades to the events. Starting with these nominally processed event lists, extraction of the order counts involved several more test-specific steps.

First of all, the test segments in the DCM data (Table 1) still contain a number of energies depending on the the number of DCM steps performed. The single energy events were extracted and written into separate energy lists with a well defined exposure time. In the EIPS tests, the data were extracted for times in which the source was turned on; the rest of the data were used to extrapolate the background count rate.

Next, we spatially extract each order by using the grating dispersion relation

$$sin(\theta) = \frac{m\lambda}{p}, \tag{3}$$

where m is the order of diffraction (an integer 0, $\pm 1, \pm 2, ...$), p is the grating period and θ is the dispersion angle. Knowledge of the dispersion axis and the grating-to-detector distance, the Rowland spacing, allows a conversion of the angle θ to a physical location on the detector of the center of the ring images.

There can be flux losses when a single order hits a gap between CCD devices. The effect is quite prominent when it occurs and the probability of an effect is high since the diameter of an order image is more than 5 mm in the MEG and about half that size in the HEG at 40 mm intrafocal position. Flux losses sometimes amounted up to 45% in the case of the HEG. Therefore every time an image partially hit a gap (the gap is about 0.43 mm wide) we calculated the portion of the rings (note that at lower energies the image always had 2 rings from 2 contributing shells) and applied this portion as a correction factor to the flux. The method, however, has its flaws, *e.g.* when the gap was between a FI and BI device, which in the low and in the high energy domain have significantly different quantum efficiencies. However, the systematic errors introduced in these domains were less than 1% and thus disregarded. Another potential flaw is where the extracted line is sitting on top of a continuum which is not flat over the size of the ring. This could result in an over- or undercorrection of the lost gap counts. This larger problem was compensated for by increasing the size of the error bars in the final calculation.

Each extracted order has a pulse height spectrum from its location on a particular CCD (Figure 7). The primary peak is visible at 1.487 keV, and pile-up peaks are visible in the pulse height spectrum at twice the energy (2 incident photons) and three times the energy (3 incident photons). For energies below 3 keV it is possible to detect higher order pulse heights corresponding to up to 4 photons hitting the same event detection cell. The corresponding number of counts was summed up and added back to the single photon count rate. The final estimated rate is

$$R = \sum_{i=1}^{4} i r_i, \tag{4}$$

where 4 is the maximum number of peaks considered, i is the peak number, and r_i is the count rate for the i^{th} peak.

Piled-up photons are identified by peaks in the pulse height spectrum at two or more times the incident energy. One major obstacle in this filtering process is, for example, that, in the DCM data, at energies below 2 keV, the 1^{st} orders in HEG and MEG spatially mix with higher orders of the W lines generated by the DCM. For energies around 1 keV this emission interferes with the first pile-up peak in the pulse height spectra. This is a particular problem in 0^{th} order, where pile-up is more significant.

These corrections were sufficient for the DCM data, where the count rates were relatively low, and there was little continuum and overlapping contamination lines. They were also sufficient for the HiREFS data, where the count rates were also low, but data suffered from overlapping orders. In this case, zero pile-up was assumed to discriminate between the overlapping lines from different orders. Figure 8 shows the pulse height spectrum for the extracted counts of a MEG-1 line from H-HAS-EA-10.004. There is a primary peak at 642 eV, and two other peaks, which look like pile-up peaks, at 1.284 and 1.926 keV. These peaks are actually the HiREFS 2^{nd} and 3^{rd} order lines of 642

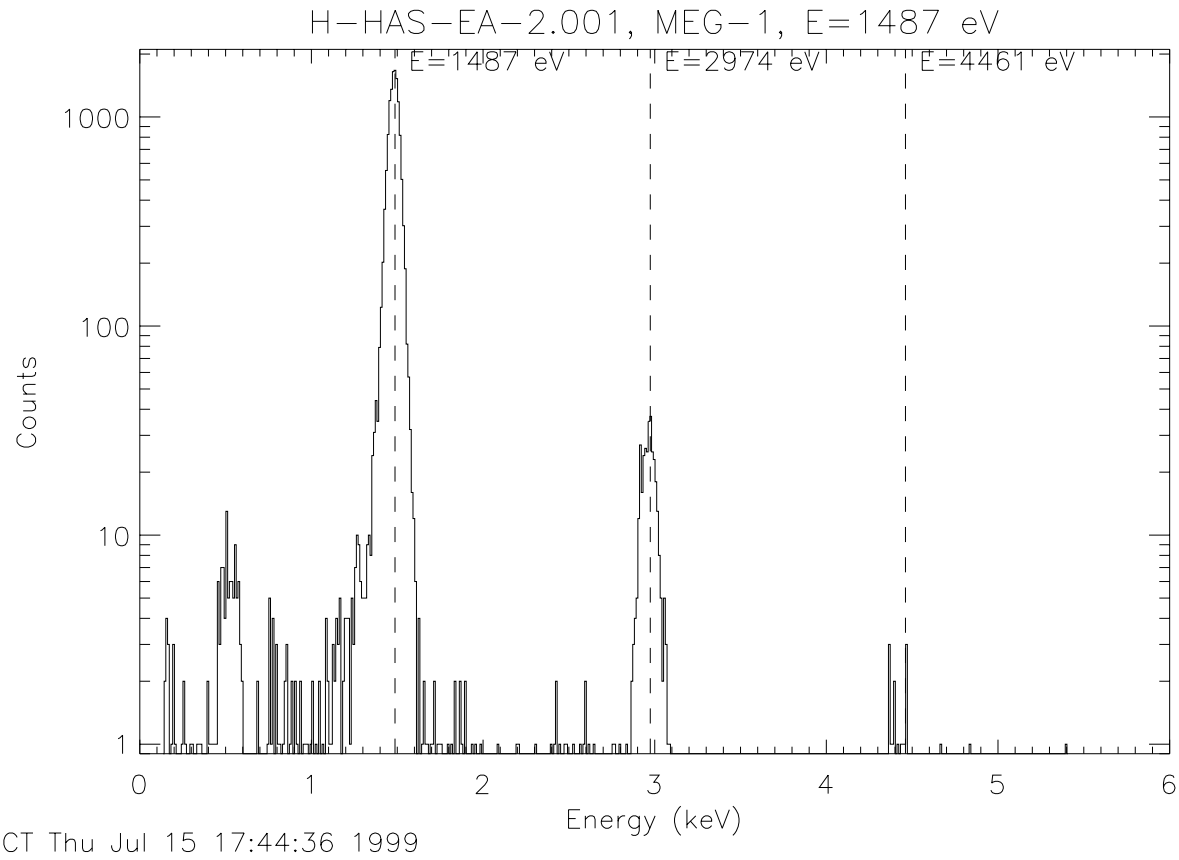

Figure 7. An example of a piled-up spectrum. This shows the pulse height spectrum for Al Kα, with the primary peak at 1.487 keV, and pile-up peaks at 2.974 and 4.461 keV.

eV. Because this effect manifests itself in exactly the same way as pile-up (see Figure 7), it was necessary to assume zero pile-up. The count rates for the HiREFS data are about 20% those of the DCM data, so this is a reasonable assumption.

In the EIPS measurements, however, the increased count rates and overlapping lines are a problem. The higher fluxes increase the pile-up fraction, which can be corrected byfirst identifying higher order pile-up peaks in the pulse height spectrum, and then summing up the corresponding number of counts to get back to the single photon count rate. A fraction of the charge is registered on the CCD during read out, resulting in a trace of counts in the read out direction. The events from that trace were added to the line flux.

4.2. Beam Normalization

In order to monitor the source flux illuminating the telescope, a system of beam normalization detectors were positioned in the facility.[19] One set was positioned close to the x-ray source, and one set at the entrance plane of the HRMA. For our analysis we are primarily interested in the flux at the HRMA entrance plane; the beam is quite large at that stage, therefore we need to determine the source flux at various positions within the beam in order to compensate for nonuniformities in the beam. Four gas flow proportional counters (FPCs) were placed at +Z (FPC-T, top), -Z (FPC-B, bottom), -Y (FPC-N, north), and at +Y (FPC-S, south) of the HRMA aperture at a radial distance of slightly larger than the outer shell radius. The denominations 'top', 'bottom', 'north', and 'south' reflect the actual orientation within the test chamber at XRCF. The analysis of the FPC data for the DCM scans has been performed by the Chandra project scientist team at MSFC. For details of this analysis we refer to the AXAF Project Science Calibration Report and references therein.[16,18]

Figure 9 shows the flux at the four BNDs during each of the 70 energy steps of the DCM separated into a diagram for lower and for higher energies. The behavior of the beam flux in the two energy domains is quite different. The reason

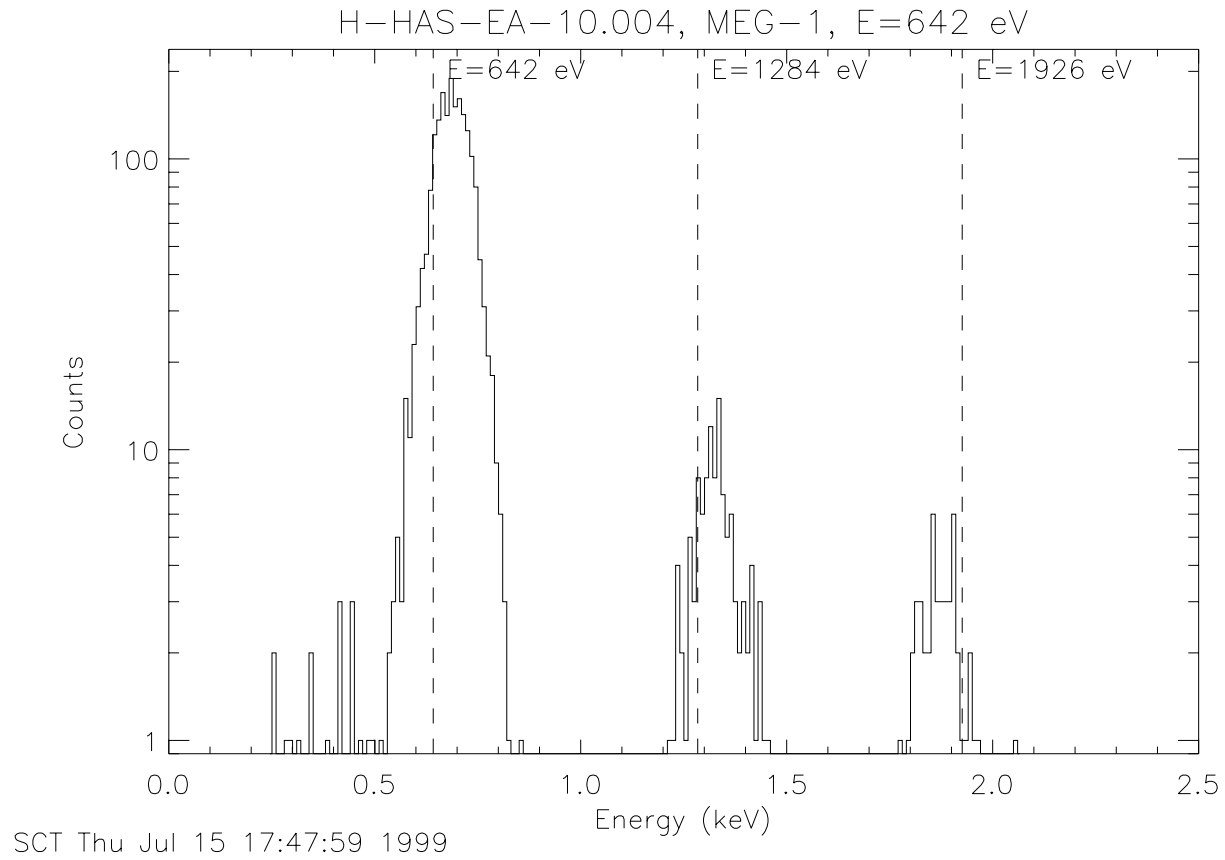

Figure 8. An example spectrum from HiREFS data. The primary peak is at 642 eV, and the peaks at 1.284 and 1.926 keV look like they might be pile-up peaks, but are HiREFS 2^{nd} and 3^{rd} orders.

for this lies in the DCM and its x-ray source. As described above, between 1.3-2.0 keV three prominent lines appear in the spectrum. The intrinsic optical properties of the DCM crucially imprint onto the uniformity of the beam: the lines will appear at only certain angles, which translate to different locations at the HRMA entrance plane. Hence the lines result in strong nonuniformities. The DCM then was tuned in a way that the major gradient in line flux appeared between FPC-S and FPC-N, while the other two remained in reasonable agreement, i.e only one a one-dimensional gradient appeared across the beam. At higher energies the four monitors are well in agreement, major discontinuities in the flux versus energy function appeared only when the crystal type in the DCM was changed. The BNDs for the DCM tests were analyzed by the Project Science Analysis Team.

Figure 10 shows the average flux of the four BNDs during each of the 5 EIPS tests. The points at 525 eV, 615 eV, and 705 eV were computed using the total flux for all three lines plus continuum (supplied by C. Allen as SAO, as described in Allen *et al.*[2]) and the measured relative fluxes of each component as seen by the HETGS. The same is true for the data at 811 eV and 930 eV. For the other points, this procedure was used to separate the line counts from the continuum counts in the BNDs. This method is described in detail in section 5.2. The error bars on each point represent the total uncertainty in the BND flux after this method has been applied.

This additional computation is required because the energies of the contaminating lines are close to the primary energy, and the BNDs are not able to resolve the different components. Figure 11 shows the pulse height spectrum for H-HAS-EA-6.002, where three lines at 525, 615, and 705 eV are sitting on a continuum. The BNDs are not able to resolve these lines, and, therefore, when the software tries to fit the three, the result is inaccurate.

The BNDs for the HiREFS tests were analyzed by the Project Science Analysis Team, and showed large non-uniformities in the beam. As a result, they developed a model for the beam uniformity, took the measured fluxes for each of the BND detectors, and computed the flux for each quadrant of each HRMA shell (see file:

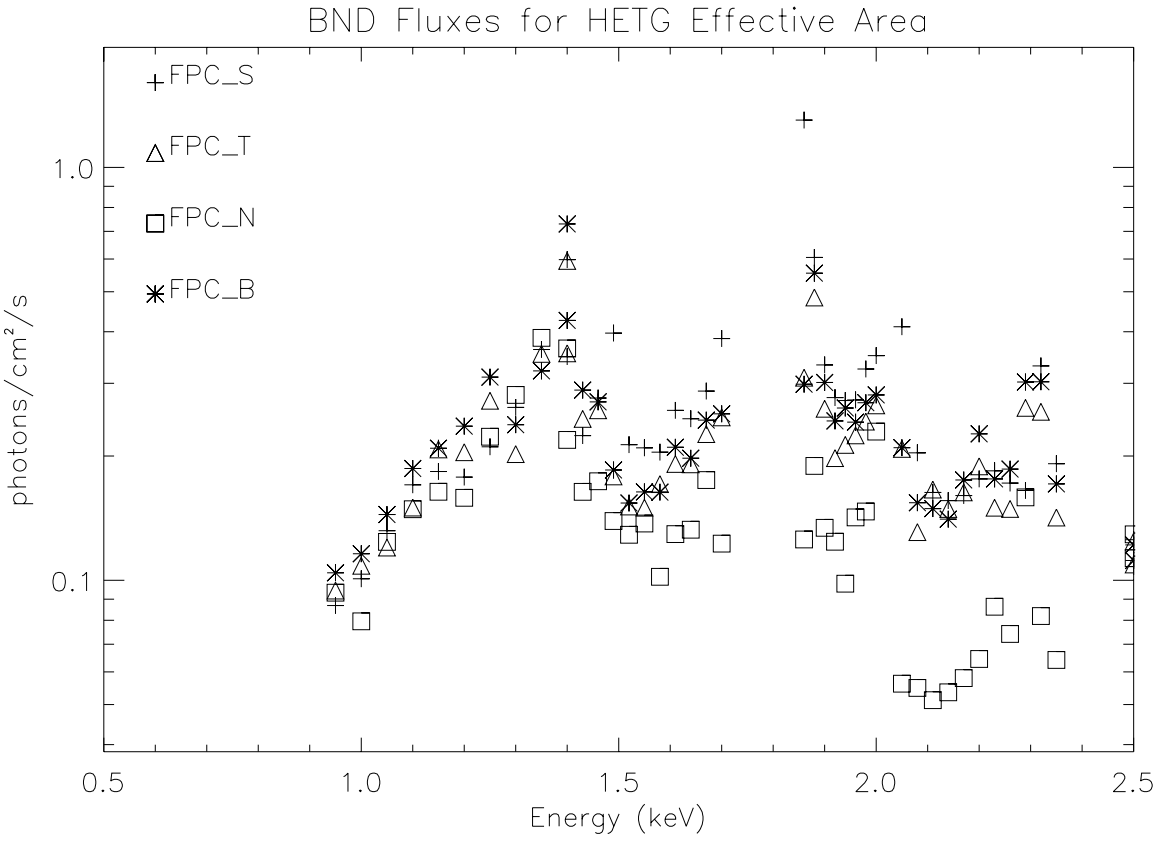

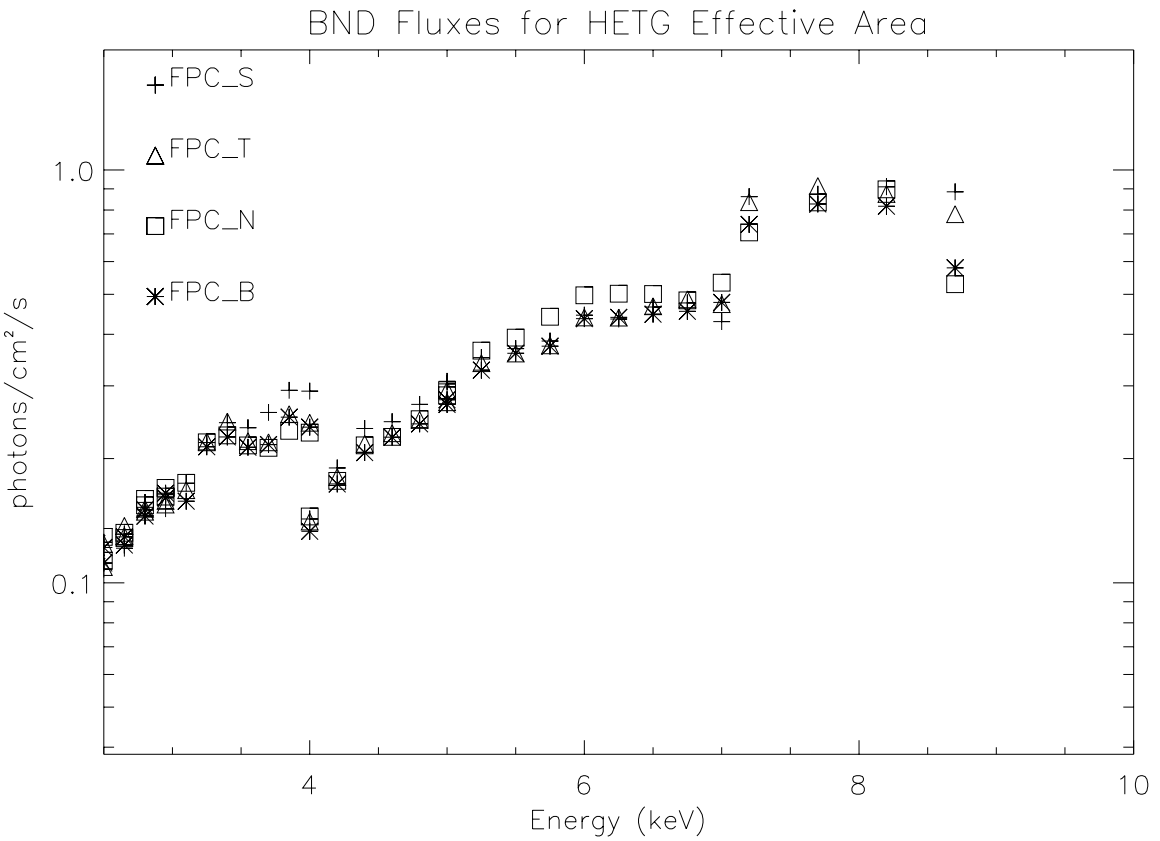

Figure 9. BND flux at the HRMA aperture as a function of energy below and above 2.5 keV for the DCM measurements.

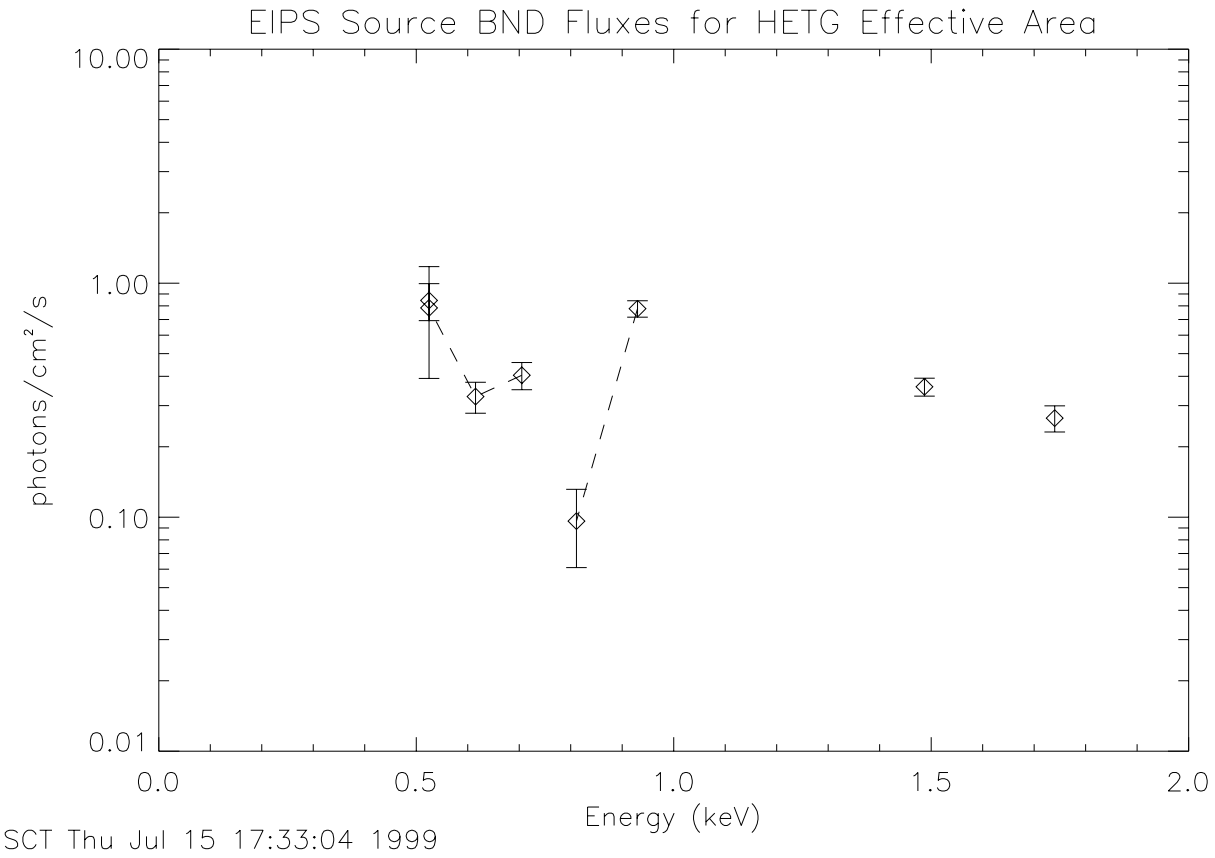

Figure 10. Mean BND flux at the HRMA aperture as a function of energy for the EIPS measurements. The error bar on each represents the total uncertainty in the flux.

`$CALDBaxafcal/xrcf/cmp/hrf_bu1_out_N19990208.rdb`). The effective flux for each grating is the sum of the four quadrants and the appropriate shells (1 and 3 for MEG and 4 and 6 for HEG), weighted by the effective area, and then divided by the total effective area. For example,

$$flux_k = \text{rasI} \times \text{norm}k \times \frac{\sum_{i,j} si\text{HRMAq}jk \times Aeff_{ij}}{\sum_{i,j} Aeff_{ij}}, \tag{5}$$

where i is the shell number, j is the quadrant number, k is the line number, rasI is the x-ray source current in mA, norm$k$ is the normalization factor of line k, and siHRMAqjk is the relative HRMA shell i, quadrant j, flux in line k. Figure 12 shows the resulting fluxes per unit area for MEG and HEG, as computed by `$CALDBaxafcal/hetg/software/ddidl/xrcf/hirefs_fluxes.pro`.

5. EFFECTIVE AREA ANALYSIS

Equation 2 gives the method used for computing the effective area. Now that we have described the method for determining each of the components, we are ready to put them together. We will first present the results from the DCM measurements, in the energy range of 0.9 to 8.7 keV. Then we will look at the results from the EIPS and HiREFS, in the energy range of 0.5 to 1.8 keV.

5.1. DCM Effective Area

5.1.1. Effective Area in 0^{th} Order

The treatment of the effective area measurements for the 0^{th} order is in many respects different from the ones for 1^{st} and higher orders. First of all, these data sets were not designed for this kind of analysis because in order to get

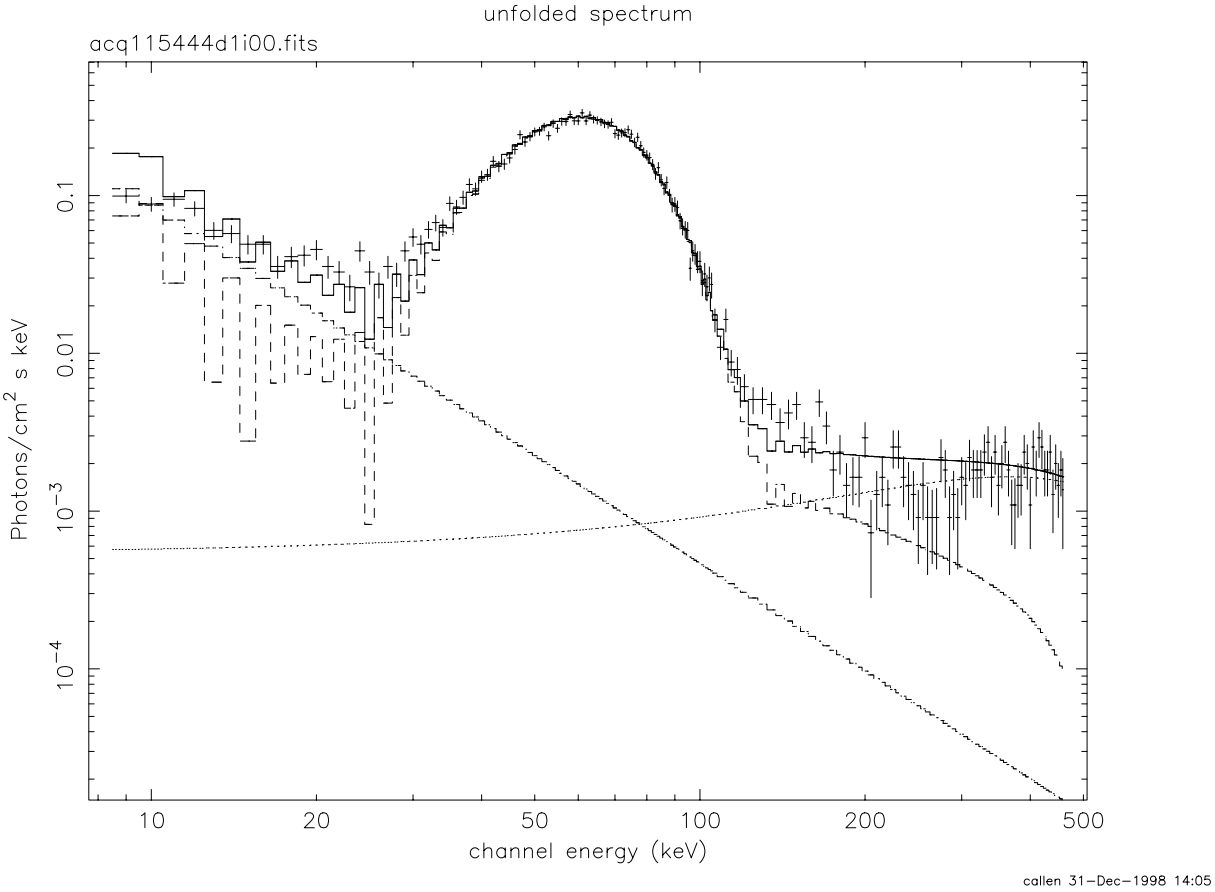

Figure 11. BND pulse height spectrum for H-HAS-EA-6.002. The lines at 525, 615, and 705 eV cannot be resolved. Please note that the x axis has been labeled improperly. The units are not keV.

sufficient statistics in the higher orders, the source flux had to be high, especially at high energies. Therefore the 0^{th} order data will be entirely dominated by pile-up effects in the CCD. Second, we are not able to separate the MEG and HEG detected events throughout the entire energy band. This is because in order to avoid any confusion of the higher order image rings with each other, the detector array was gradually moved back into the focal plane above 2.5 keV. Figure 6 shows the 0^{th} order image as it appeared between 2.5 and 4.0 keV. In this image, the detector was already moved back from 40 mm out of focus to 20 mm. It is clear that a separation of the inner two rings from the outer ones, in particular, separating the images of mirror shells 3 and 4, would already introduce a significant systematic uncertainty. Above 4.0 keV, where the out-of-focus position was 10 mm and less, the separation of the inner rings would have become impossible. Therefore we will analyze the 0^{th} order data for two reasons: first, we use the low energy domain in order to fine tune the beam normalization in the range between 1.3 and 2.5 keV; second to attempt a pile-up treatment using results from the ACIS affective area analysis performed by CXC ACIS team.[2]

The BND measurements in the top diagram of Figure 9 show quite a strong gradient between FPC-S and FPC-N flux, indicating strong beam nonuniformities. In the range 2.0 - 2.5 keV the FPC-N, however, shows an unusually large drop in flux. In order to minimize this effect on the analysis of the higher orders, we attached a weighting factor to FPC-N in the range between 1.3 and 2.5 keV.

$$BND = \frac{FPC\text{-}T + FPC\text{-}B + FPC\text{-}S + (w \times FPC\text{-}N)}{4} \tag{6}$$

Then we simply tuned this weighting factor, w, until the data in this range matched the values just below 1.3 and just above 2.5 keV. The result is shown in the top diagram of Figure 13. This factor was then used for the higher orders.

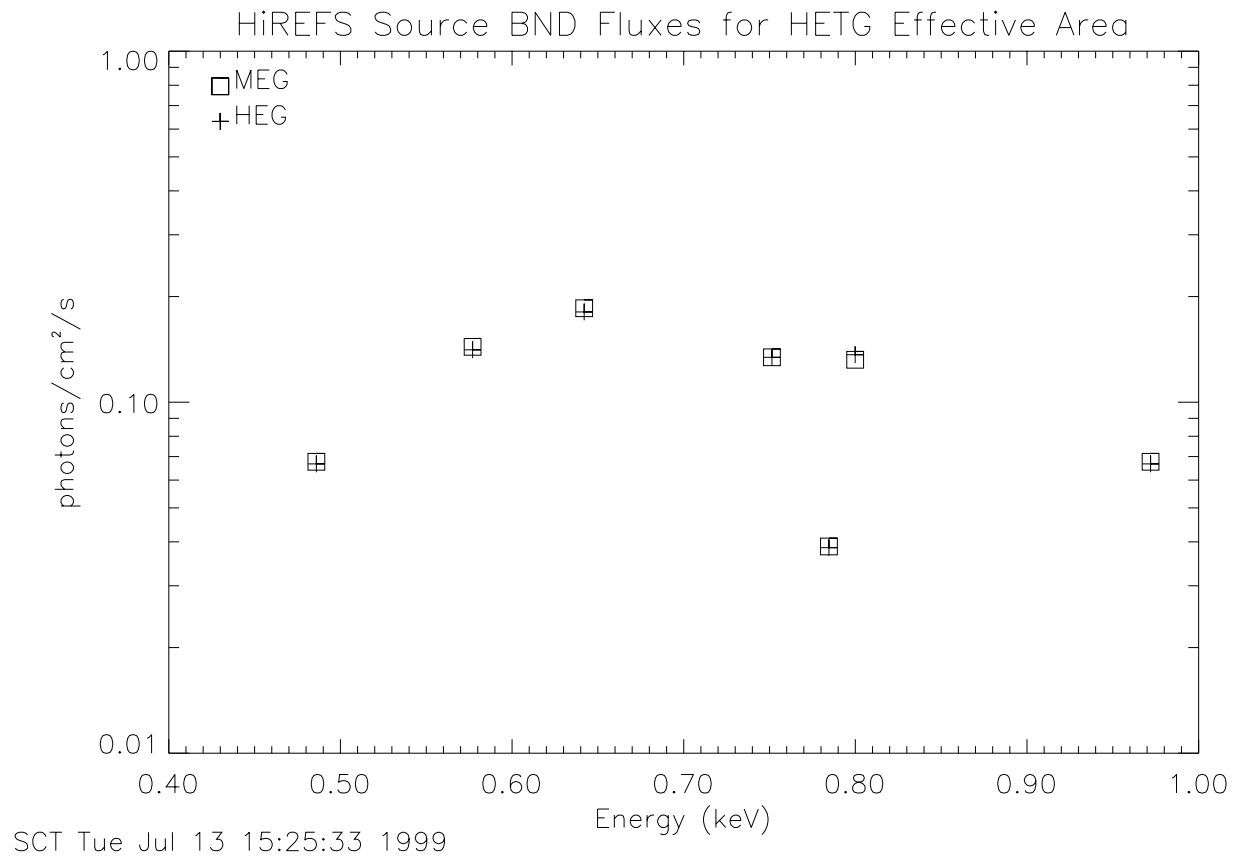

Figure 12. BND flux at the HRMA aperture as a function of energy for the HiREFS measurements.

For the other portions of the energy band, the normalization flux was simply the average over all four BNDs. Below 1.3 keV we observed an agreement with the expectation of better than 5%, between 1.3 and 2.0 keV the uncertainty is determined by the scatter induced by the BND uncertainties and thus can reach 30%; between 2.0 and 3.0 keV it is again near 5%.

For the 0^{th} order focal plane events, standard pile-up correction, Equation 4, has been applied to produce the top plot in Figure 13. Clearly above about 3 keV this procedure starts to fail because higher order pulse heights fall beyond the maximum pulse height channels. We, therefore, observe a large drop in the measured effective area. In a first attempt to estimate the amount of piled-up photons, we fit the ratio of the non-piled-up fraction to the measured piled-up fraction in the range 0.9 to 2.5 keV. In this range we were able to recover piled-up photons for up to 4 photons hitting an single detection cell. This could be done by a power law ($E^{0.27}$).

We extrapolated this function into the high energy range and added that flux to the count rate above 2.5 keV by substituting into Equation 4. The final rate is then

$$R = r_1(1 + E^{-0.27}), \tag{7}$$

where r_1 is the rate in the primary (non-piled-up) peak and E is in keV. We also had to take in account that the source flux above 2.5 keV increased by a factor of 8 and scaled that function simply by that increase. The resulting area was still short of the expectation by up to 45%. Allen *et al.*[2] found that some of the piled-up photons migrate into ASCA grade 7, i.e. outside the chosen standard grade set. This results in another energy dependent correction factor. We thus calculated the grade migration correction factor for our data sets following the recipe given by Allen *et al.*[2] and applied it to the data. Again the result above 6 keV was still short by about 20%. Allen *et al.* 1998 also apply a correction for lost charge and undetected events. Above 6 keV, we simply applied those correction factors from Table 1 the ACIS Effective Area Report[2] for the case of S3. The result can be seen in the bottom diagram of

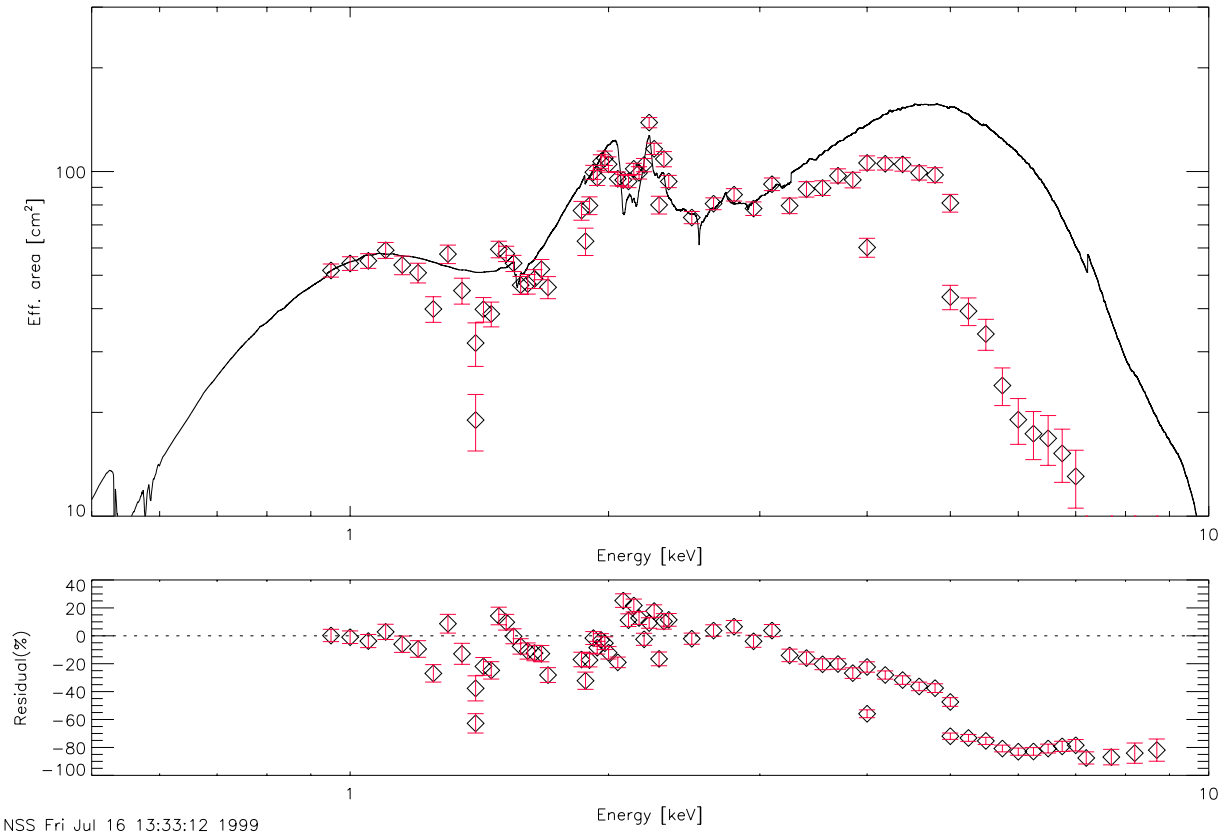

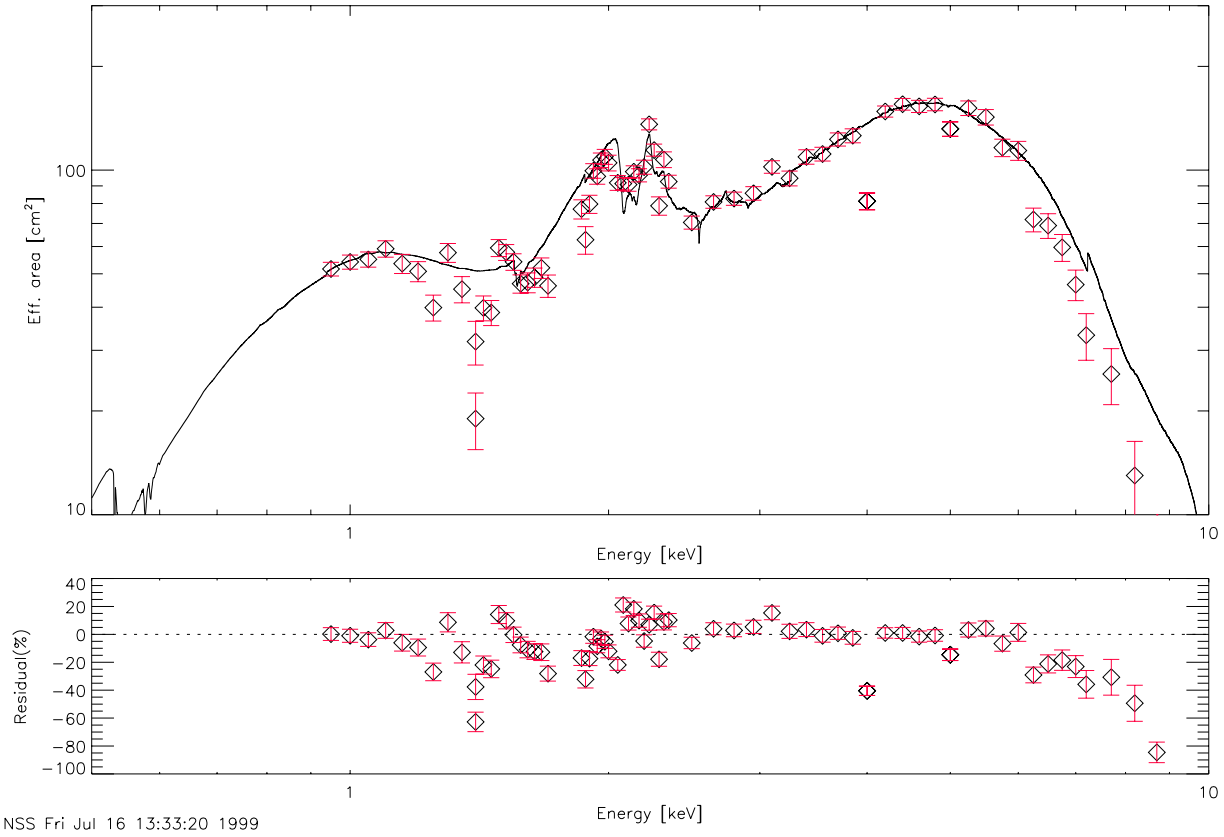

Figure 13. Comparison of the measured and modeled effective area for the combined 0^{th} order of MEG and HEG as a function of energy. The top (bottom) diagram shows the result without (with) pile-up correction as described in the text. Included under each plot is the residual from the model, in percent.

Figure 13. The area now seem to fit the expectation, although a clear overcorrection is visible. However, we have to emphasize, since we did not in particular determine the lost charge correction for our own data sets, the result is merely an estimation. It however demonstrates that those corrections applied by Allen[2] are indeed necessary and in a reasonable order of magnitude. The applied corrections introduce additional systematic errors to the data, which are *not* reflected in the error bars in the bottom diagram of Figure 13.

5.1.2. 1^{st} and 3^{rd} Order Effective Areas for the MEG

The MEG is optimized to suppress efficiency in even orders. In the following we do not present results for any even MEG order. The top diagram of Figure 5 shows the grating efficiencies for the 0^{th} orders for MEG and HEG, the middle plot has $\pm 1^{st}$ order for MEG and HEG, and the bottom has $\pm 3^{rd}$ order for MEG and $\pm 2^{nd}$ order for HEG. For most energies, the MEG and HEG $\pm 1^{st}$ order efficiencies are approximately 10 times those of MEG $\pm 3^{rd}$ order and HEG $\pm 2^{nd}$ order, respectively.

Considering this fact, we should not expect a significant contribution from pile-up effects for single 3^{rd} orders for the MEG. In the 1^{st} order single side efficiencies, however, we do have to expect a similar amount of piled-up photons at energies below 2.2 keV as we observed in 0^{th} order, since the efficiencies are of comparable magnitude. At higher energies the efficiencies are between a factor 5 and 15 lower, which reduces the probability of pile-up accordingly. In the following we, therefore, will not apply any other correction than to add all the counts found in detected higher pile-up orders in the pulse height spectra (Equation 4).

Figure 14 shows the effective areas determined for the -1^{st} (top) and +1^{st} (bottom) order of the MEG. All data points are confined within 3 CCDs, S2-4. The -1^{st} order covers S2 for all energies below 4.2 keV, and S3 for all higher energies, the 1^{st} order covers S4 for energies below 1.5 keV, and again S3 for all the higher energies. In both orders it is clear that measurements around the Tungsten Mα line at 1.75 keV (width $\sim$ 150 eV) have to be disregarded; although we are able to clean the focal plane data from that emission, we cannot entirely do so in the BNDs. Around 1.3 keV we see some scatter in the data, which is also induced by the uncertainty of the BNDs of the order of 10 to 20%. At all other energies, with a few exceptions, we measured the effective area to an accuracy of 5 to 10%. At high energies above 6 keV counting statistics do not allow a determination better than 10%.

We compare these measured effective areas to the modeled effective area from Equation 1. To 1^{st} order we find a remarkable match of the data to the model. However, there are notable deviations, which are at the limit or exceed the 5% uncertainties of the data points. For both plots, the very low energy data points stay below the expectation by an amount of somewhat less than 5%.

Figure 15 shows the areas determined for the MEG 3^{rd} orders. Again, except for a couple of data points, the general trend shows that the measured values match nicely the expectation. However, the statistics already limit the significance to less than 20%. For our initial look at higher orders, please refer to the paper by Flanagan *et al.*[10]

5.1.3. 1^{st} and 2^{nd} Order Effective Areas for the HEG

The middle and bottom diagram of Figure 5 show the the grating efficiencies for 1^{st} and 2^{nd} HEG orders. The 2^{nd} order efficiency, comparable to the 3^{rd} order efficiency in the MEG, is low enough to ensure that results will be not be affected by pile-up. For the 1^{st} order, we face a similar situation to the MEG 1^{st} order, i.e. pile-up is sufficiently corrected for by adding just the 2-photon peak in the pulse heights back to the measured count rate. This peak is detectable throughout the whole band pass.

Figure 16 shows the effective areas determined for the -1^{st} (top) and +1^{st} (bottom) order of the HEG. Note, that the HEG has considerably less efficiency below 2.5 keV than the MEG. Therefore, counting statistics are worse than in the MEG. Below 1.5 keV we cannot determine the effective area better than 20%, above 1.5 keV and below 5 keV the uncertainties are of the order of 10-15%. Again, the range around 1.75$\pm$0.15 keV is not reliable and should be disregarded.

Within the given uncertainties, the measured values again fit quite well with the model. However, a major effect is observed above 4 keV in both orders. Figure 9 shows that at this energy the FPC-T and FPC-N switch in relative intensity. The switch may result from a spatial nonuniformity of the beam, which would affect the HEG more than the MEG due to the smaller HEG entrance aperture. The MEG -1^{st} order does show a similar trend at 5 keV, but at much lower scale. Another more likely reason for this apparent drop in EA is due to grade migration. This is an effect which occurs at higher count rates and energies, where events from the standard grade set (0, 2, 3, 4, and 6) tend to migrate into higher number grades. The HEG $\pm 1^{st}$ orders have the highest count rates per unit area, and

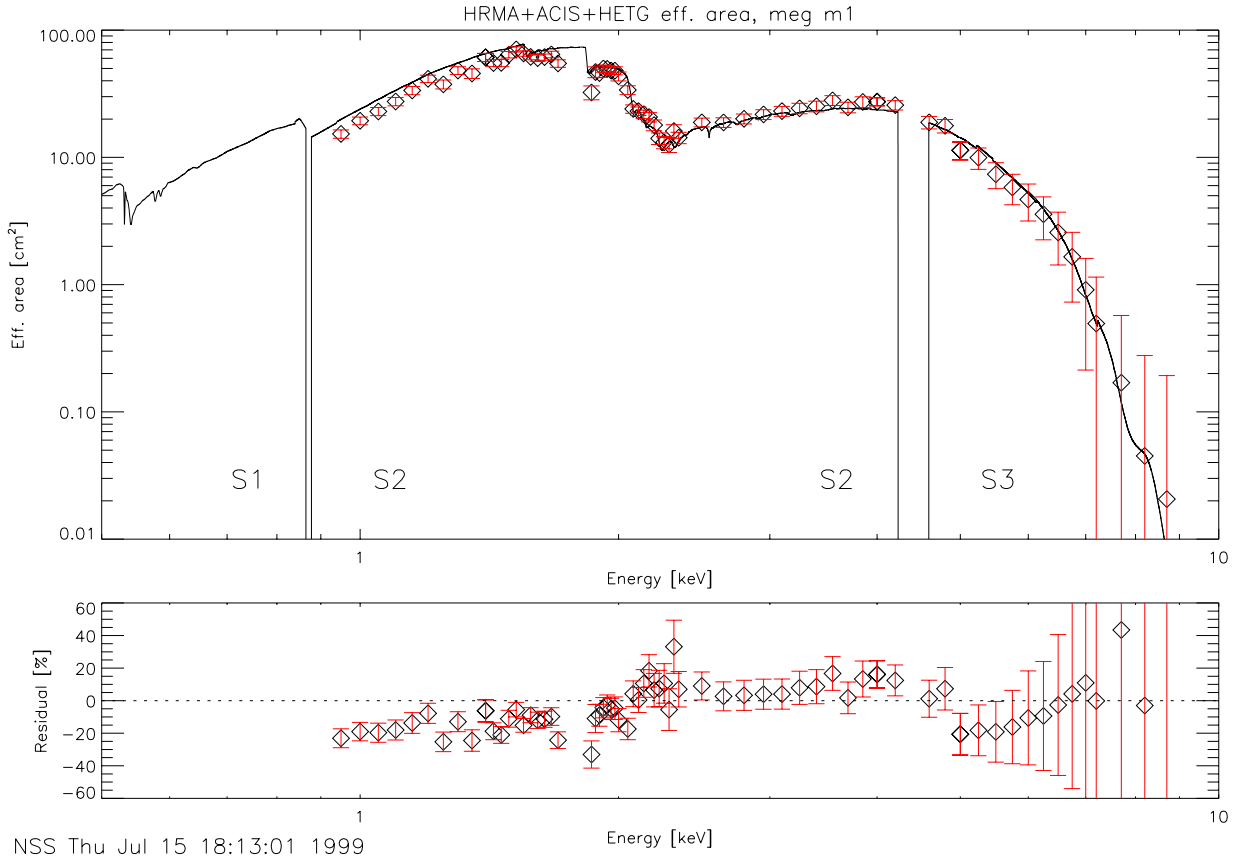

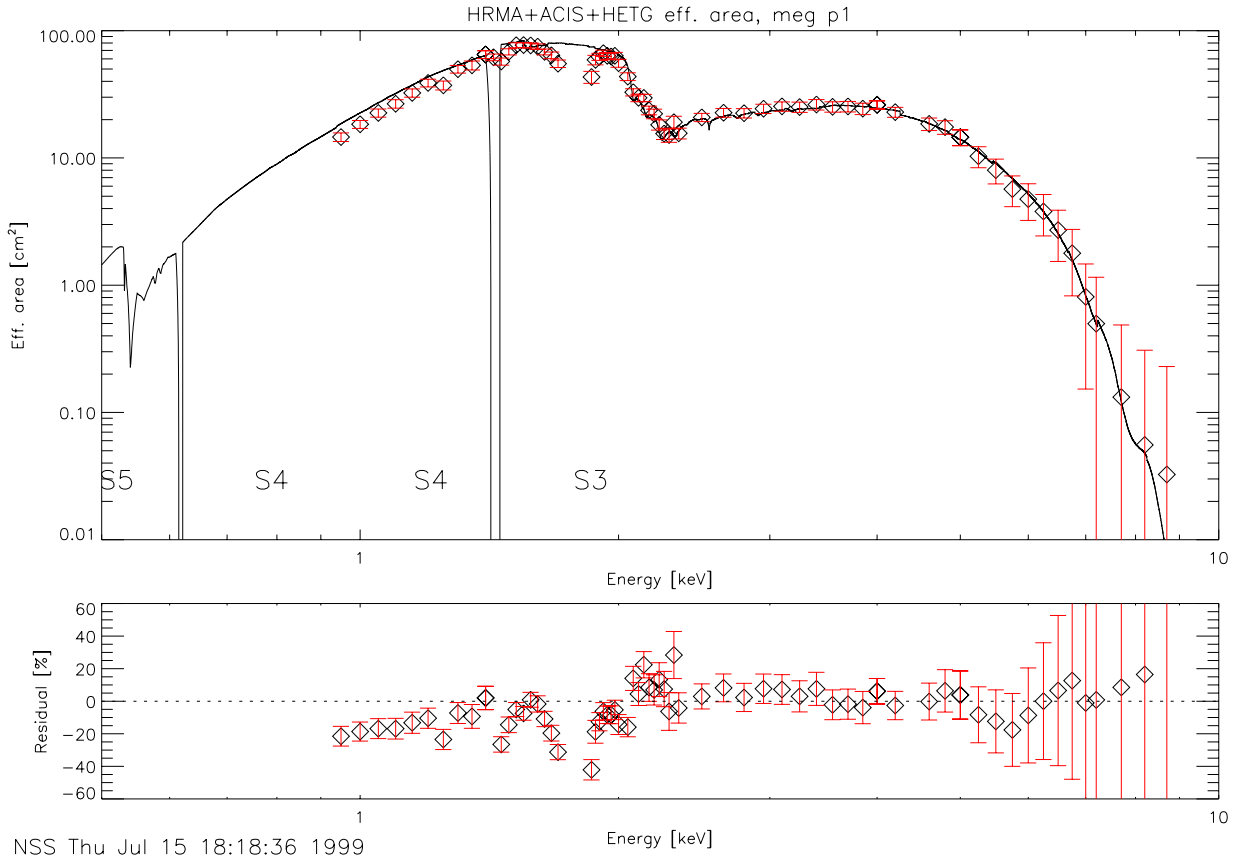

Figure 14. Comparison of measured absolute effective areas from the DCM data at XRCF of the MEG 1^{st} order to the modeled effective area. Negative orders cover S2 and S3 (from low to high energies), the gap appears just above 4 keV. Positive orders cover S4 and S3 with the gap at 1.5 keV.

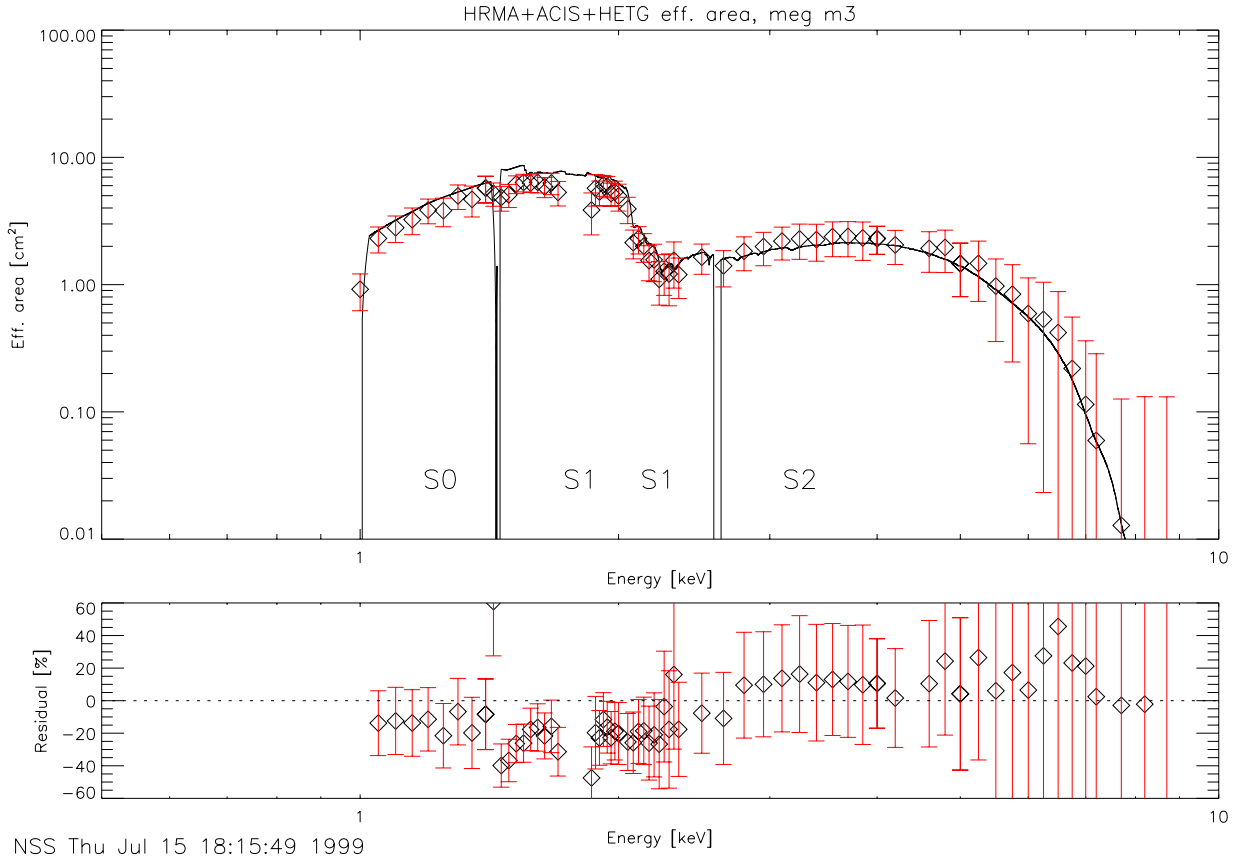

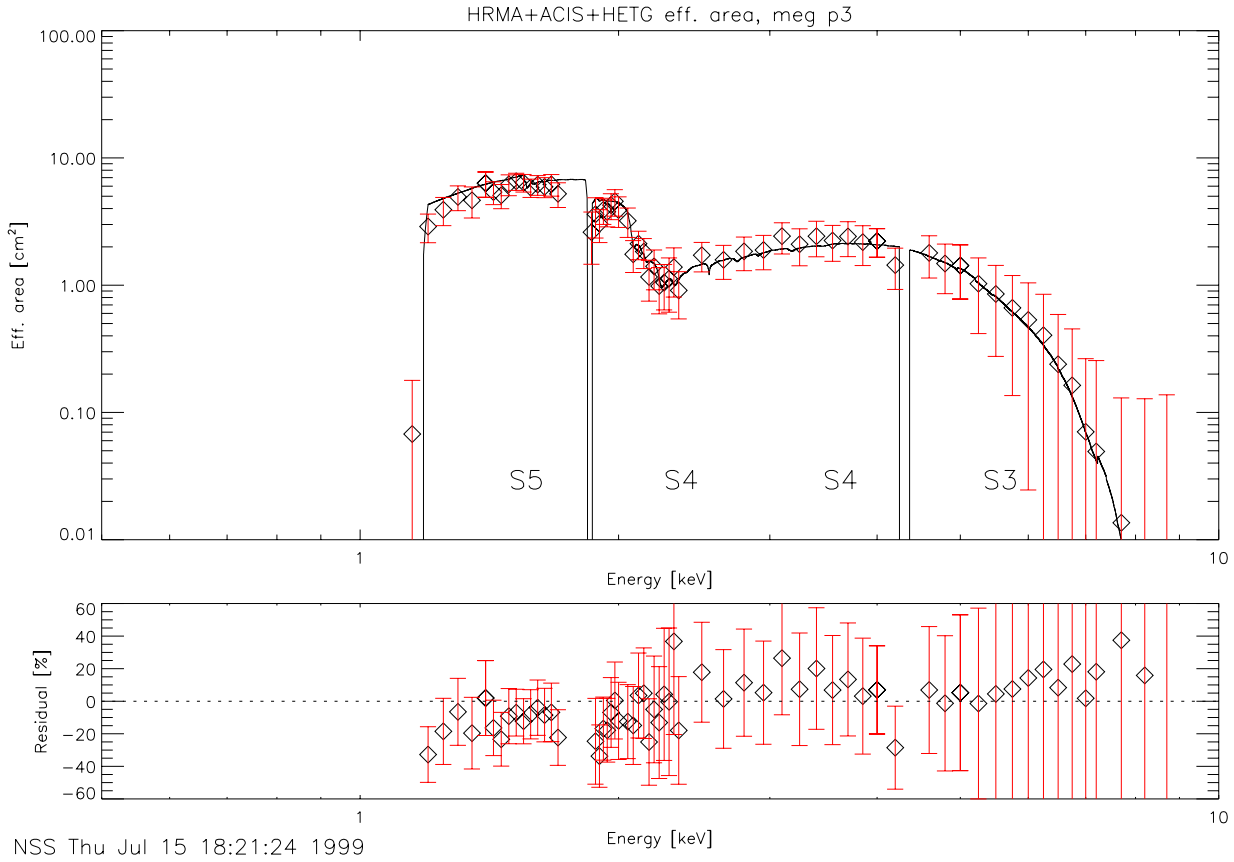

Figure 15. Comparison of measured absolute effective areas of the DCM data at XRCF of the MEG 3^{rd} order. Negative orders cover S0, S1, and S2 (from low to high energies), the gaps appear at about 1.3 and 2.4 keV. Positive orders cover S5, S4, and S3 with the gaps at 4.1 keV.

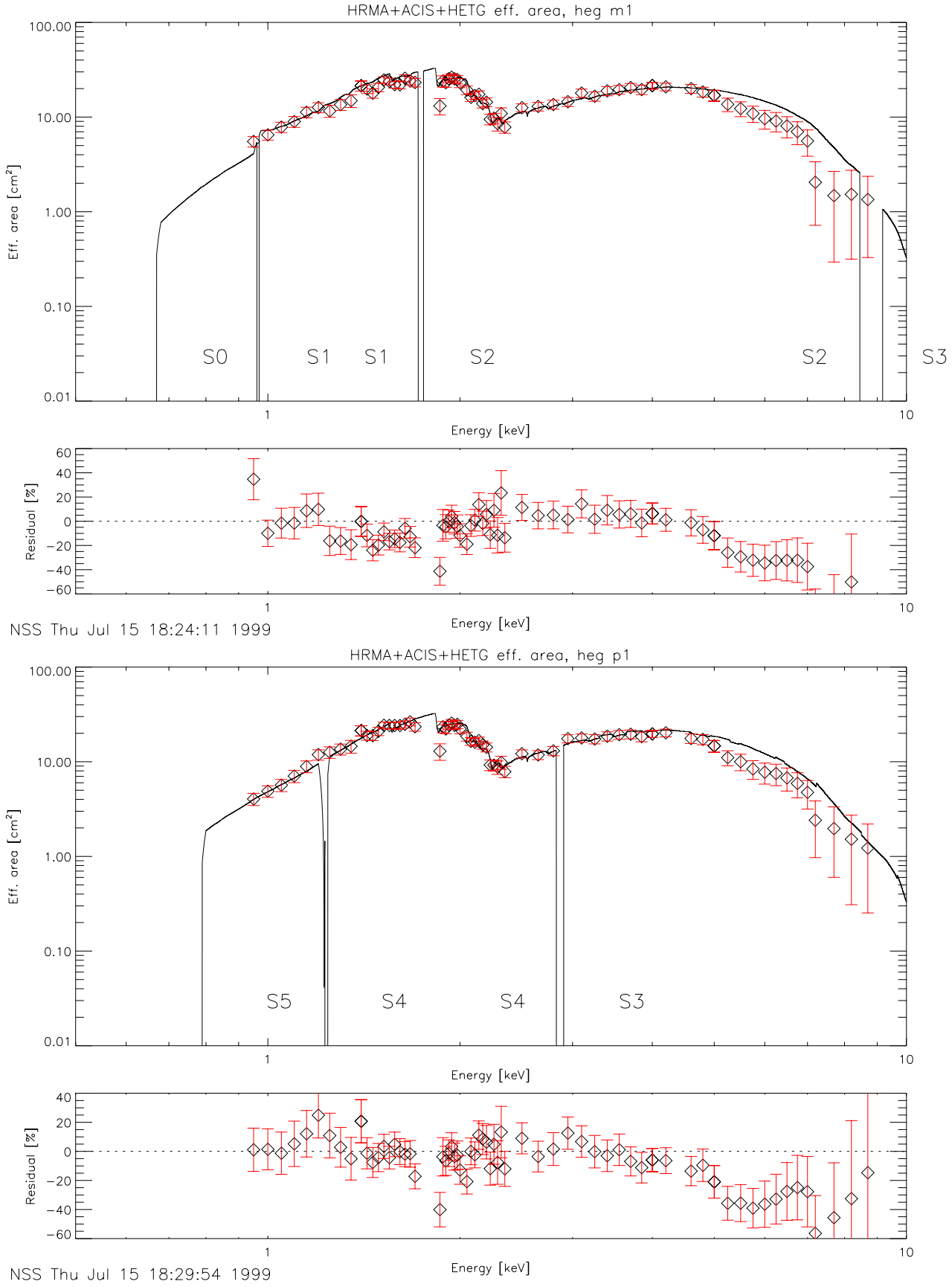

Figure 16. Comparison of measured absolute effective areas of the DCM data at XRCF of the HEG 1^{st} order to the modeled effective area. Negative orders cover S1 and S2 (from low to high energies), the gap between the two appears 1.7 keV. Positive orders cover S5, S4, and S3 with the gaps at 1.3 and 2.9 keV respectively.

therefore, this effect is most prominent there. A smaller effect can also be seen in MEG $\pm 1^{st}$ orders, where the count rates are high, but events are spread over more pixels. Two methods for correcting for grade migration are discussed in detail in section 6.

Figure 17 shows the areas determined for the HEG 2^{nd} orders. The measured values match the expectation. But as observed in the MEG 3^{rd} orders, statistical uncertainties limit the significance to less than 20%. For higher order results we again refer to the report by Flanagan.[10]

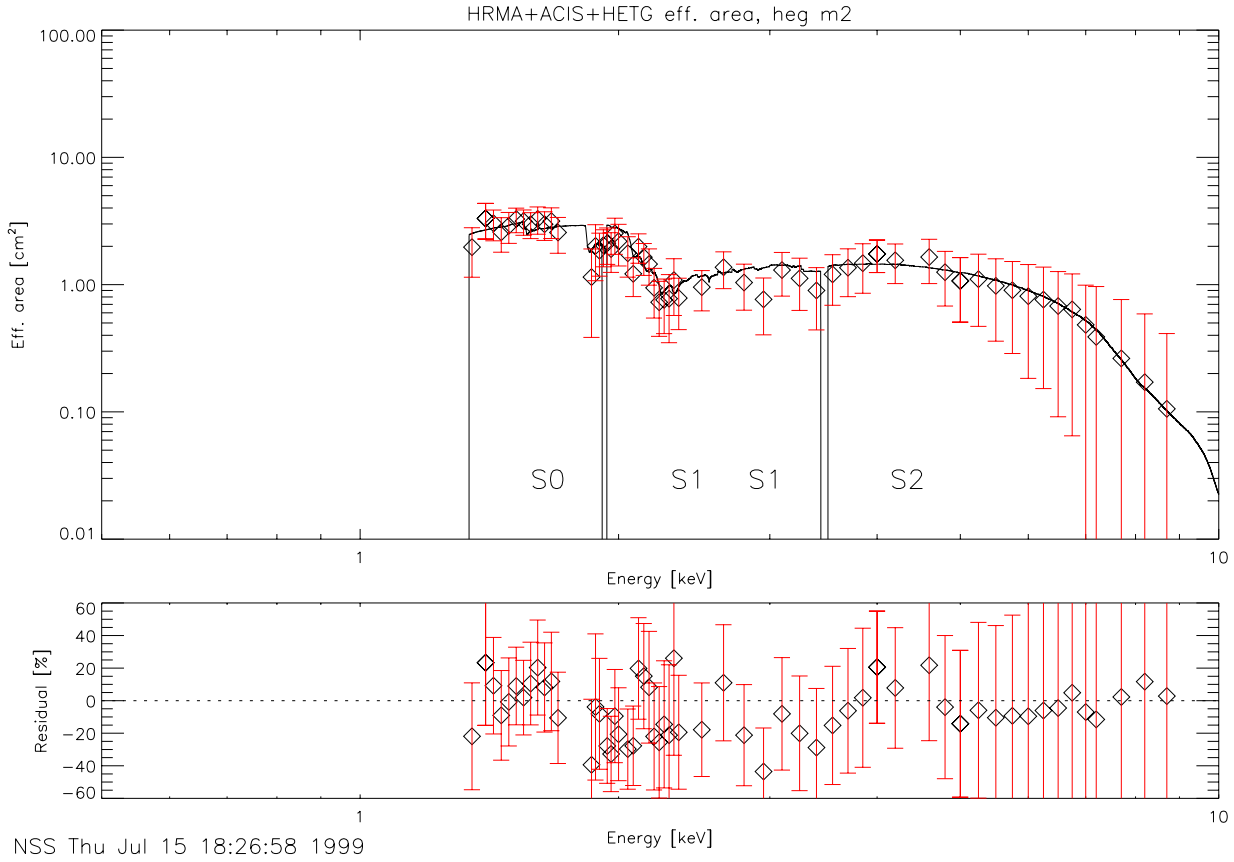

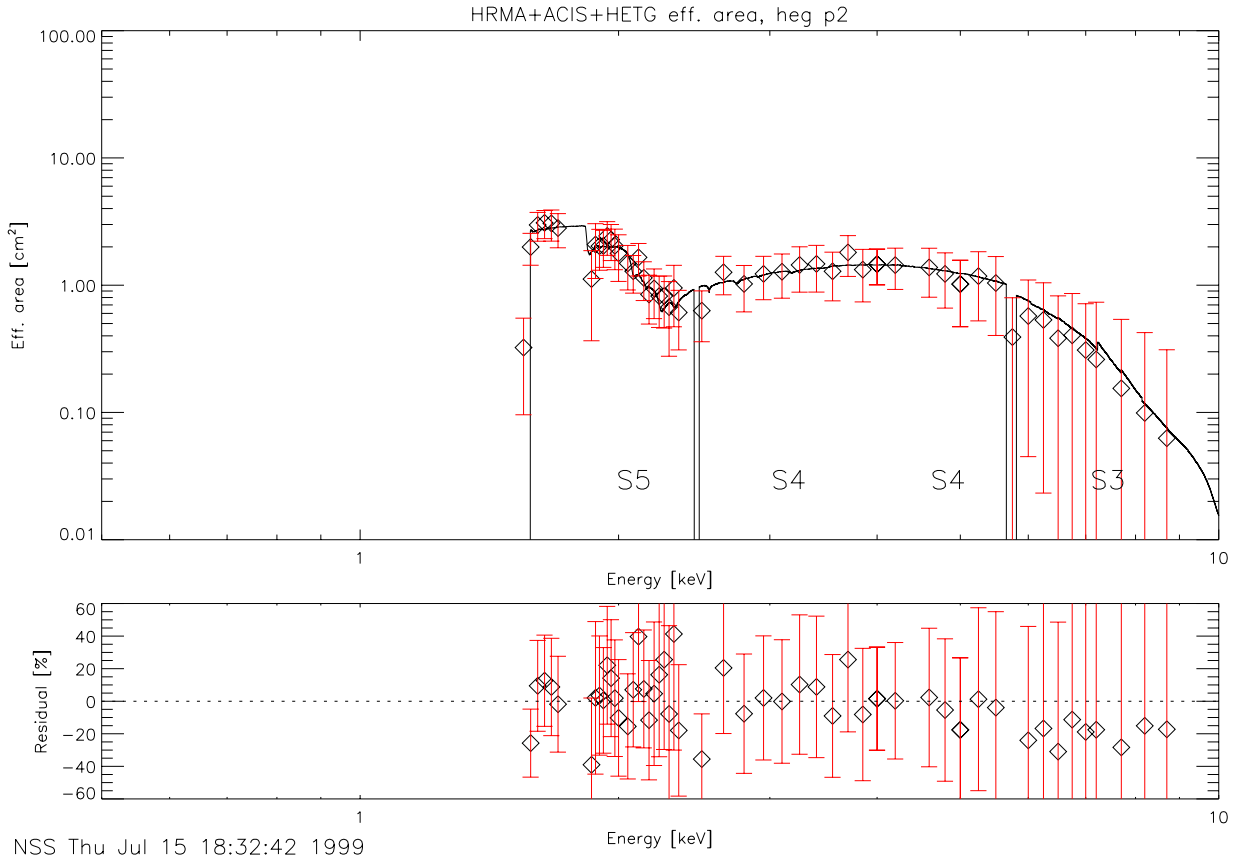

Figure 17. Comparison of measured absolute effective areas of the DCM data at XRCF of the HEG 2^{nd} order. Negative orders cover S0, S1, and S2 (from low to high energies), the gaps between them appear at about 1.9 and 3.2 keV. Positive orders cover S5, S4, and S3 with the gaps at 2.2 and 5.8 keV respectively.

5.2. EIPS and HiREFS Effective Area

For the HiREFS measurements, a similar procedure for computing the effective area for the DCM measurements was also used, with a few minor changes. First is the calculation of the source flux, using the beam uniformity model developed by the project science analysis team (Equation 5). Second is the assumption of zero pile-up (Figure 8). These two corrections increase the uncertainty of the final calculation, but the effect is quite small. The contributions to the overall uncertainty in the measured effective area for the HiREFS data are

- statistical uncertainty in the ACIS counts for each line
- corrections (gap and trace counts) in all counts
- uncertainty in counts due to shift in extraction ring
- BND fit uncertainty
- beam uniformity fit uncertainty
- a factor for the assumption of zero pile-up ($\sim 3\%$)

Additional corrections need to be applied to the EIPS data that are not necessary with the DCM or HiREFS data because the latter have well separated monochromatic lines. A major correction is the separation of each of the lines from the surrounding continuum and from contaminating lines, both in the focal plane detectors and the BNDs. The separation in the focal plane data is relatively straightforward, using the pulse height energy.

For the BNDs, where the energy resolution is much worse, a more involved approach was required to estimate the flux in each line, by making use of the HETGS measured counts. The first step takes the focal plane count rates at a given energy and converts them into flux units. This relation is

$$F_{HETGS}(E_i) = \frac{R_{HETGS}(E_i)}{A_{HETGS}(E_i)}, \tag{8}$$

where $R_{HETGS}(E_i)$ is the HETGS count rate at energy E_i and $A_{HETGS}(E_i)$ is defined in Equation 1. From $F_{HETGS}(E_i)$, the relative flux fraction in each component is determined:

$$f_{HETGS}(E_i) = \frac{F_{HETGS}(E_i)}{\sum_{i=1}^{N} F_{HETGS}(E_i)}, \tag{9}$$

where N is the total number of features (lines or continuum) for that file. Using these fractions, the relative fractional BND count rate can be calculated by applying the appropriate quantum efficiency of the BND detectors at each energy.

$$r_{BND}(E_i) = \frac{f_{HETGS}(E_i) QE_{BND}(E_i)}{\sum_{i=1}^{N} [f_{HETGS}(E_i) QE_{BND}(E_i)]} \tag{10}$$

These relative strengths are then used to assign a BND count rate, $R_{BND}(E_i)$, that corresponds to each single feature.

$$R_{BND}(E_i) = R_{BND}(total) \times r_{BND}(E_i) \tag{11}$$

To convert these to flux, one must divide by the quantum efficiency and effective area of the BNDs.

$$F_{BND}(E_i) = \frac{R_{BND}(E_i) r_{BND}(E_i)}{QE_{BND}(E_i) A_{BND}} \tag{12}$$

Finally, a mean of the four BND fluxes was taken to compare with the extracted count rate per unit area from ACIS.

$$F_{final}(E_i) = \frac{F_{BND-N}(E_i) + F_{BND-S}(E_i) + F_{BND-T}(E_i) + F_{BND-B}(E_i)}{4} \tag{13}$$

Any errors which may have arisen from nonuniformities in the beam were accounted for by increasing the uncertainty in the final calculation.

This additional computation for the EIPS tests results in a more complex error analysis. The contributions to the overall uncertainty in the measured effective area for the EIPS data were the uncertainties in each of the components mentioned in Equations 8 through 13. These are

- statistical uncertainty in the ACIS counts and the counts for the entire order
- corrections (gap, pile-up, and trace counts) in all counts
- uncertainty in counts due to shift in extraction ring
- uncertainties in Chandra models (HRMA EA, HETG Efficiency, ACIS QE)
- BND fit uncertainty
- source nonuniformity
- uncertainty in BND quantum efficiency

Each independent source of error was quantified and then folded through by error propagation. Therefore, even though the statistical counting error is smaller for the EIPS measurements when compared to the DCM measurements, the overall uncertainty is comparable.

5.2.1. 1^{st} Order Effective Areas for the MEG

Figure 18 shows the measured effective area in MEG for the positive and negative 1^{st} orders compared to the model. The red diamonds are the uncontaminated EIPS lines of O Kα, Al Kα, and Si Kα. The green squares are lines from the EIPS files which contain contamination lines; Fe Lα, which is contaminated by Fe Ll and O Kα, and Cu Lα, which is contaminated by Cu Lζ. The blue x's are from the 1^{st} order HiREFS data, the pink triangles are from the 2^{nd} order HiREFS data, and the purple plus signs are DCM data for reference. Also included under each EA plot, is a plot of the residual percent deviation from the model. The large error bars on the 2^{nd} order HiREFS data are driven by the BND fit uncertainty, which is high due to W contamination. All sources agree with each other to within the size of their error bars. Above 1.5 keV there is relatively good agreement with the model, but for lower energies, the measured effective areas fall well short ($\sim 20\%$).

5.2.2. 1^{st} Order Effective Areas for the HEG

Figure 19 shows the measured effective area in HEG for the positive and negative 1^{st} orders compared to the model. Again, the red diamonds are uncontaminated EIPS lines, the green squares are lines from the EIPS files which contain contamination lines, the blue x's are from the 1^{st} order HiREFS data, the pink triangles are from the 2^{nd} order HiREFS data, and the purple plus signs are DCM data for reference. Included, also, are plots of the residual percent deviation from the model. In this case, most of the measured effective areas in each plot match remarkably well with the model. This is most likely because the HEG separates the lines out more in the dispersion direction than the MEG, and therefore, the contaminating lines overlap less. There is no deficiency below 1.5 keV that was seen in the MEG EAs. This suggests a problem with the MEG grating efficiency.

For the two 1^{st} order HiREFS points, the measured EAs fall short of the model, but are consistent with the EIPS data, to within the size of the uncertainty. For the HEG, the defocused lines are spread over less pixels than for the MEG. So this is probably where the assumption of zero pileup breaks down. In the 2^{nd} order HiREFS point at 0.8 keV matches well with the model and is consistent with the surrounding data.

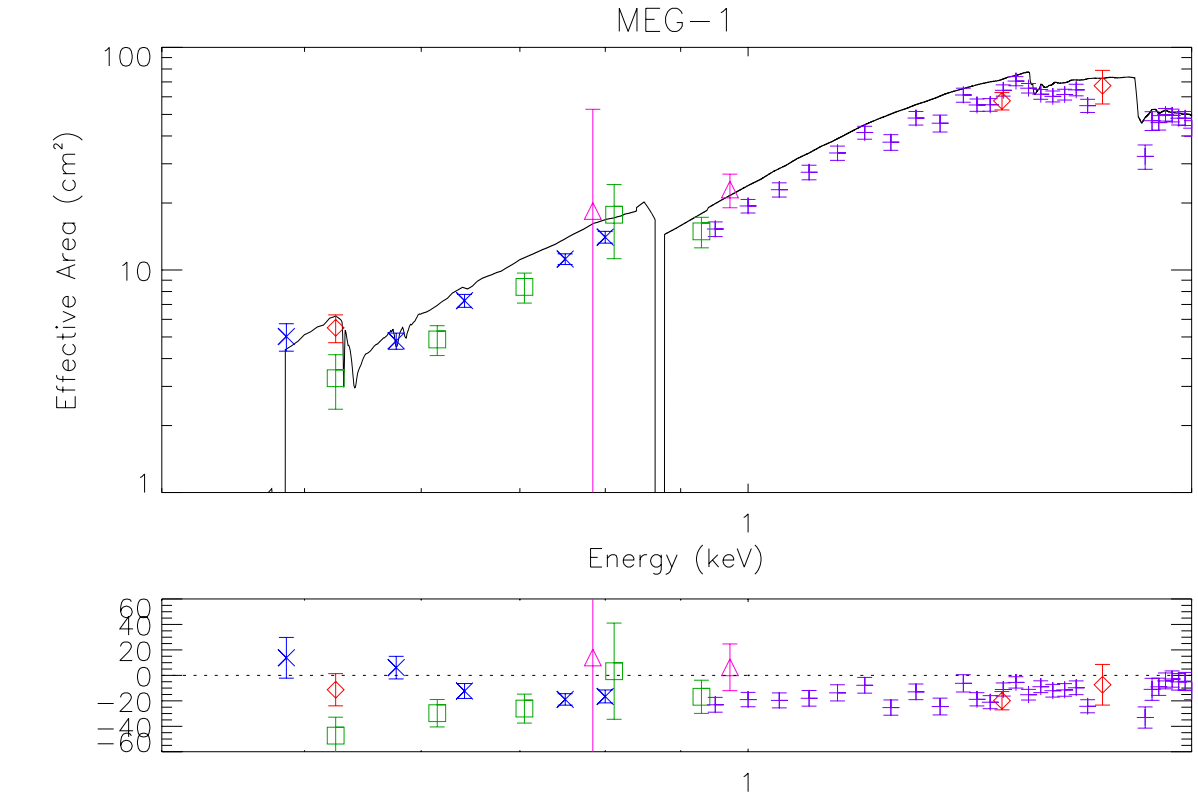

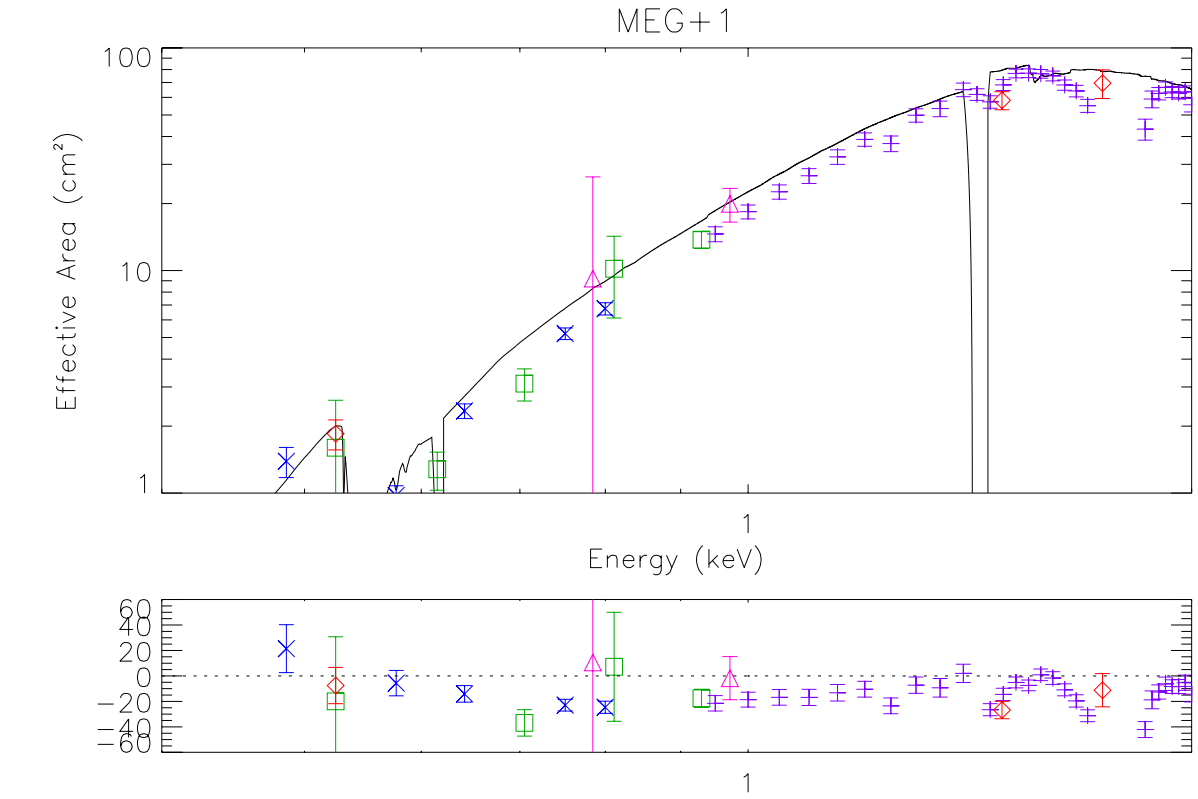

Figure 18. Comparison of measured absolute effective areas of the EIPS and HiREFS data at XRCF of the MEG 1^{st} order to the modeled effective area. Negative orders cover S1 and S2 (from low to high energies), and positive orders cover S5, S4, and S3. The first and third plots show the measured and modeled effective areas, while the second and fourth show the residual percent deviation from the model.

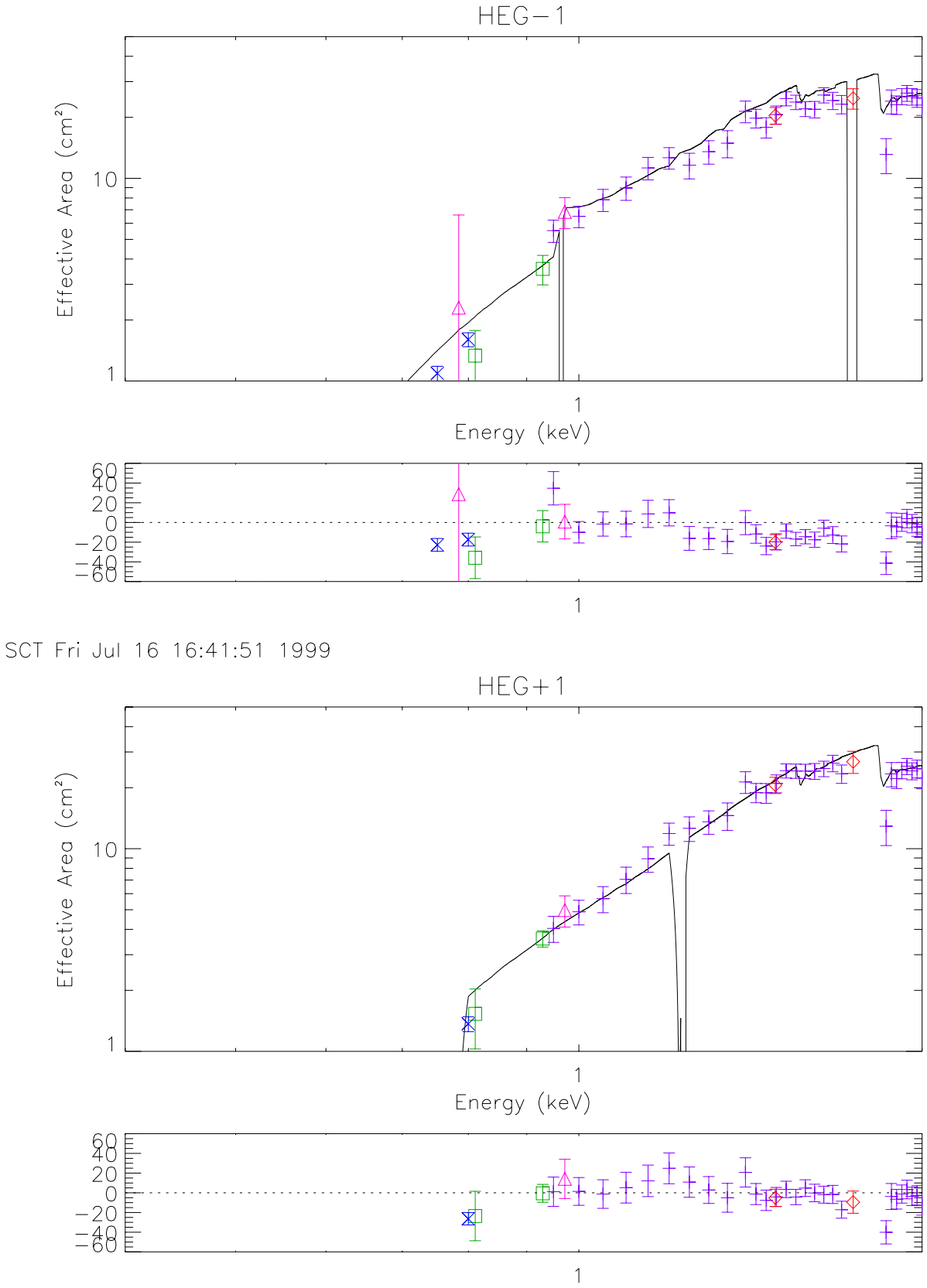

Figure 19. Comparison of measured absolute effective areas of the EIPS and HiREFS data at XRCF of the HEG 1^{st} order to the modeled effective area. Negative orders cover S0, S1, and S2 (from low to high energies), and positive orders cover S5 and S4. The first and third plots show the measured and modeled effective areas, while the second and fourth show the residual percent deviation from the model.

6. GRADE MIGRATION

With higher count rates and increasing energy, events which may have appeared in the standard grade set (0, 2, 3, 4, and 6), tend to migrate into higher number grades, causing the non-standard grades (1, 5, and especially 7) to have more events. This is generally due to two or more events with overlapping charge clouds, or a larger charge cloud from a single event. If there are two events and they occur within one integration cycle, then they will be interpreted by the detection software as one event over more pixels. The ratio of the events in the standard grade set to the events in all grades is called the "Branching Ratio" (BR).

$$BR = \frac{C_{G02346}}{C_{All\ Grades}} \tag{14}$$

In the limit of zero count rate and low energy, this ratio is close to 1, but for higher count rates and energies it decreases. This will result in an apparent loss in effective area, as seen at energies above 4 keV in Figure 16, and, to a lesser extent, Figure 14.

6.1. Simple Correction

As a first attempt to correct for this effect, we applied the same technique that was used by the ACIS team, as described by Allen *et al.*[1] That is, using sub-assembly ACIS data taken during the instrument calibration phase in 1997 at the CCD laboratory at MIT in a single chip (non-flight) configuration, in which each CCD was uniformly illuminated by an x-ray source at fairly low count rates. These tests were designed to screen each CCD for performance and relative efficiencies and thus the data should be closest to the derived CCD quantum efficiencies. A comparison of their branching ratios to the branching ratios from DCM data taken during phase H should give a first order correction for grade migration changes observed in the DCM data. For the energies that didn't match the ones used during sub-assembly testing, a linear interpolation was used. The correction was then applied to the final measured effective area. This method, however has its limitations and does not fully account for the energy and count rate dependence of grade migration and sub-assembly sources were heavily contaminated. Tables 4 and 5 summarize these correction factors.

6.2. Count Rate Correction

We, then, attempted to use the sub-assembly data to approximate the zero count rate dependence limit for branching ratios. The phase H data have average count rates up to 700 counts/cm^2/s for the HEG 1^{st} order and 300 counts/cm^2/s for the MEG 1^{st} order. The count rates in the sub-assembly data range from 60 to 160 counts/cm^2/s over the entire array (I0 and I3 for FI devices and S3 for BI). In the case of the HEG, these count rates are almost an order of magnitude lower. Also, the count rates from the phase H data are average rates over the extraction region, and will have local count rates which are even higher. In the case of the MEG the rates are a factor of 3 lower and we first assume that these rates are low enough to be near the zero count rate dependence limit. Figure 20 shows the BR versus count rate for the sub-assembly data and Table 6 lists the average BR for I0, I3, and S3. The top and middle plots of Figure 20 show how the FI device sub-assembly branching ratios vary with count rate. Although less pronounced in the case of I0, BRs in the two FI chips appear to increase with increasing count rate indicating that at least for FI CCDs the sub-assembly data are not near the zero count rate limit and may not be used for to correct for grade migration.

During phase "I" at XRCF calibration only involved the ACIS flight instrument and EIPS x-ray sources. Three CCDs were only read out successively using the high speed tap mode, which allowed a bypass of the full read out and allowed recording from one CCD at a time. Each device in phase I, I3, S1, and S3 only, was uniformly illuminated at low count rates. Although the count rates during phase I were sometimes not significantly lower than during sub-assembly tests they have two distinct advantages: much cleaner (i.e more monochromatic) x-ray sources and the actual flight read-out electronics. Therefore they are much more suitable to represent the zero count rate limit than sub-assembly data, in order to decouple the count rate and energy dependence of the BR. Figure 21 shows the branching ratio for the phase I data plotted versus count rate. The BR at low count rates now hardly change with count rate and significant reduction appear at higher energies. To first order the BR can be expressed as

$$BR(E, R) = f(E) \times g(R), \tag{15}$$

Energy	Correction Factors					
(keV)	S0	S1	S2	S3	S4	S5
0.950	-	-	0.961441	-	0.962149	1.02686
1.00	0.966838	1.11157	0.954081	-	0.957723	0.956370
1.05	0.952383	1.03791	0.955784	-	0.955920	0.953963
1.10	0.954451	1.04343	0.952873	-	0.954706	0.949829
1.15	0.980163	1.06623	0.956189	-	0.956940	0.964598
1.20	0.992084	1.10170	0.956521	-	0.954234	0.958844
1.25	0.938411	1.13093	0.957284	-	0.959096	0.938173
1.30	0.933439	1.11154	0.963737	-	0.938161	0.932225
1.35	0.925148	1.10568	0.969628	-	0.949114	0.930043
1.40	0.924555	1.13927	1.00007	-	0.961013	0.930383
1.43	0.919222	1.09014	0.960858	-	0.941340	0.924043
1.46	0.917000	1.11262	0.945828	-	0.925721	0.942852
1.49	0.924043	1.10994	0.950038	-	0.927936	0.937192
1.52	0.925455	1.13846	0.944899	-	0.937585	0.921783
1.55	0.943037	1.11029	0.951027	-	0.951828	0.927949
1.58	0.934115	1.15818	0.955991	-	0.945861	0.934115
1.61	0.940281	1.18701	0.971922	-	0.957006	0.999437
1.64	0.956660	1.18527	0.978499	1.04750	0.967057	0.953195
1.67	0.952613	1.04086	0.993709	1.06108	0.979354	0.953983
1.70	0.960747	1.05797	0.995253	1.05297	0.987699	0.966381
1.86	0.956051	1.10164	1.00563	1.09611	0.983878	0.958888
1.88	-	1.10219	1.01550	1.11101	1.00819	0.954226
1.90	-	1.08971	0.981926	1.06152	0.971642	0.952402
1.92	-	1.09523	0.976947	1.04306	0.969456	0.956555
1.94	-	1.10556	0.974565	1.05254	0.975170	0.958583
1.96	-	1.11442	0.978640	1.04430	0.966052	0.946927
1.98	-	1.21122	0.974340	1.05505	0.974800	0.950025
2.00	-	1.21323	0.981335	1.05416	0.944826	0.946733
2.05	-	1.12512	0.968796	1.03720	0.962166	0.956374
2.08	-	1.16196	0.966007	1.00328	0.955774	0.944497
2.11	-	1.02281	0.957913	0.995660	0.959852	0.960407
2.14	-	1.16550	0.960340	1.01904	0.960101	0.946767
2.17	-	1.14212	0.964746	1.00216	0.953510	0.947901
2.20	-	1.27151	0.963449	0.989605	0.949036	1.02204
2.23	-	1.05169	0.961220	0.975928	0.956847	0.978964
2.26	-	1.05282	0.961646	0.996147	0.955581	0.951306
2.29	-	1.10881	0.965692	1.00125	0.966047	0.952441
2.32	-	1.05032	0.963875	1.00345	0.953576	0.953576
2.35	-	1.26270	0.964306	0.997407	0.954711	0.954711
2.50	-	1.13785	0.974936	0.983100	0.971022	-
2.65	-	1.06563	0.984049	0.986100	0.986178	-
2.80	-	1.16350	0.964906	0.988457	0.964906	-
2.95	-	1.23681	0.964826	1.00550	0.964826	-
3.10	-	1.17283	0.995636	1.00534	0.970137	-
3.25	-	1.26452	0.987905	1.05192	0.964668	-
3.40	-	-	1.01869	1.04211	0.964588	-
3.55	-	-	0.964509	1.04705	0.964509	-
3.70	-	-	0.964429	1.05301	0.964429	-
3.85	-	-	1.01199	1.06732	0.977382	-

Table 4. Summary simple correction factors using branching ratios interpolated from sub-assembly data. They are the ratio of the BR in Sub-assembly to that of the DCM data. (part 1 of 2)

Energy	Correction Factors					
(keV)	S0	S1	S2	S3	S4	S5
4.00	-	-	1.02164	1.06932	0.975784	-
4.20	-	-	0.971639	1.06137	0.964165	-
4.40	-	-	1.02599	1.09415	0.981912	-
4.60	-	-	0.967632	1.08901	0.960569	-
4.80	-	-	0.952859	1.14437	0.952859	-
5.00	-	-	0.950282	1.08102	0.950577	-
5.25	-	-	1.12813	1.22601	0.940713	-
5.50	-	-	1.08985	1.22540	0.925964	-
5.75	-	-	0.902413	1.26341	-	-
6.00	-	-	1.06769	1.21269	-	-
6.25	-	-	0.868788	1.18610	-	-
6.50	-	-	0.855084	1.11541	-	-
6.75	-	-	0.801322	1.13739	-	-
7.00	-	-	0.769979	1.04103	-	-
7.20	-	-	1.56262	1.52981	-	-
7.70	-	-	1.49633	1.36429	-	-
8.20	-	-	1.23913	1.06961	-	-
8.70	-	-	0.614278	1.31303	-	-

Table 5. Summary of simple correction factors using branching ratios interpolated from sub-assembly data. They are the ratio of the BR in Sub-assembly to that of the DCM data. (part 2 of 2)

Chip	Mean BR
I0	0.8353
I3	0.8302
S3	0.9447

Table 6. Summary of mean branching ratios for sub-assembly data.

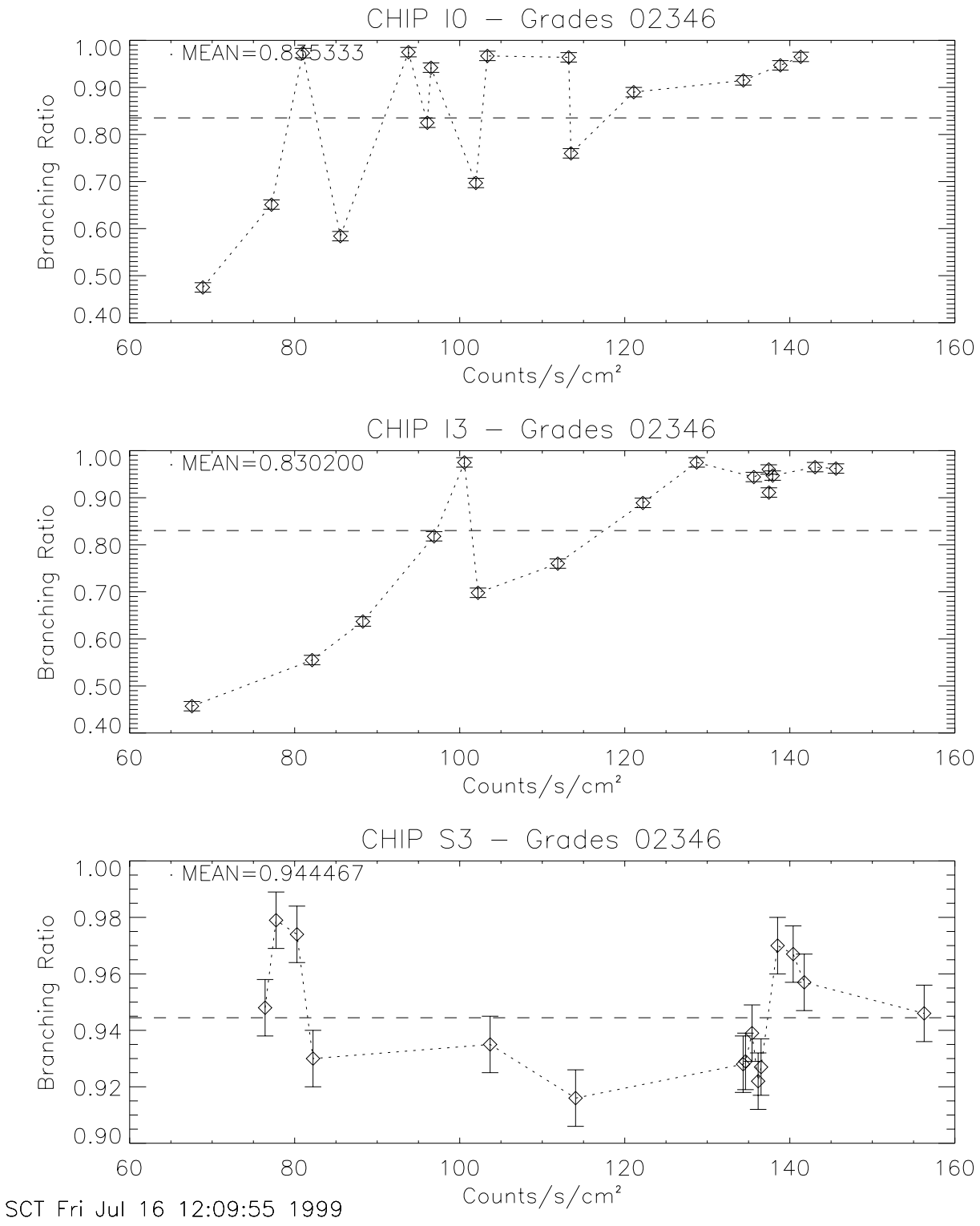

Figure 20. Sub-assembly branching ratios vs. count rate.

so, we are considering a case where $g(R)$ is approximately constant. These are trends that are expected from simple considerations involving larger charge cloud radii and thus overlaps at higher energies, i.e the change in BR in Figure 21 is not due to count rate but higher energies of the incident photons.

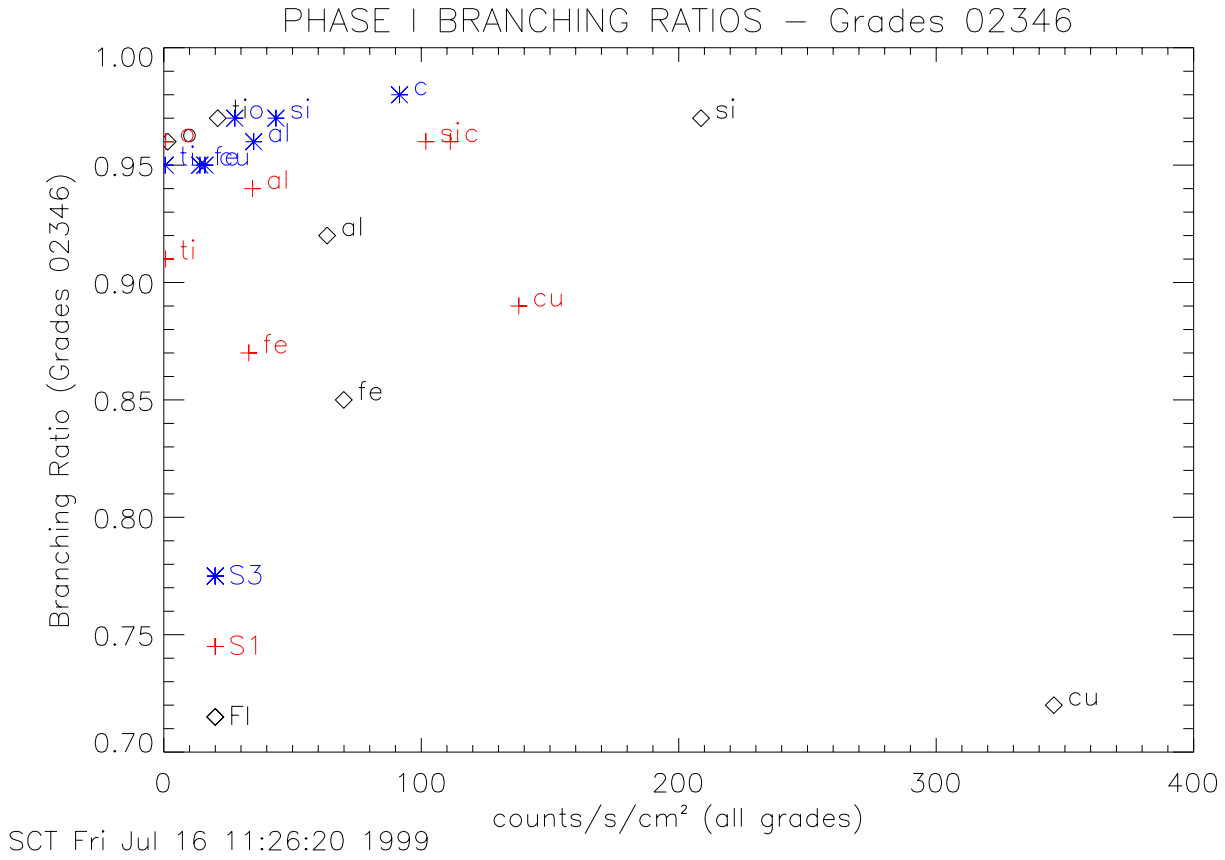

Figure 21. Phase I EIPS branching ratios vs. count rate. Data from Chip S1 is plotted with a red +, S3 with a blue $*$, and S2 (which was used for all FI chips) with a black $\diamond$.

We, therefore, plotted the phase I BR versus energy and fit the data to a polynomial. These data and fits are shown in Figure 22. For the FI chips, the data were best fit by a combination of a constant and a quadratic, while the BI chips required only a linear fit. For all three plots, the fit uncertainty is the root-sum-square of the standard deviation between the data and the fit and the average statistical uncertainty. This total uncertainty is dominated by the standard deviation component.

If this fit is $f(E)$, then g(R) is

$$g(R) = \frac{BR(E,R)}{f(E)}, \tag{16}$$

where $BR(E,R)$ is the observed BR, which is energy and count rate dependent. We can then remove the count rate dependence from the EA by dividing by $g(R)$, or multiplying a correction factor, which is

$$C(R) = \frac{1}{g(R)}. \tag{17}$$

To obtain C(R), we then evaluated the fit at the energies of the DCM phase H XRCF data, and computed the ratio of the fitted value to the measured DCM BR. These data are shown in the Figures 23 through 26, where the top plot shows the phase I fit in red and the phase H data in blue, with a different symbol for each chip. The middle plot in

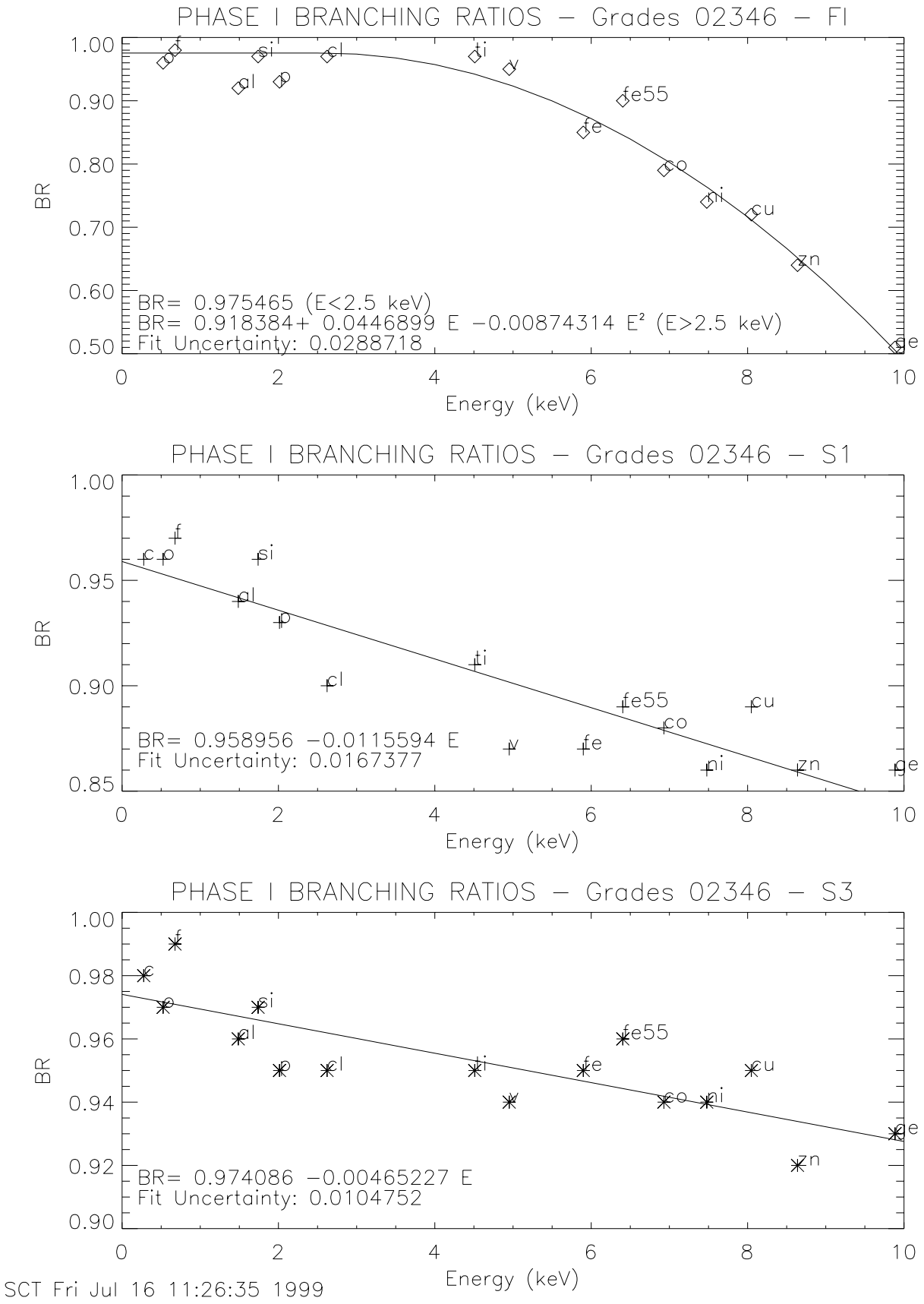

Figure 22. Phase I EIPS branching ratios vs. energy.

each of these figures shows the ratio of the phase I fit to the phase H data, as a function of energy. The bottom plot shows the same ratio versus count rate. The data were adequately fit to a line, and this equation ($C(R)$) was used as the correction factor for count rate, which will be multiplied by the final measured EA.

$$EA_{corrected} = EA_{uncorrected} \times C(R) \tag{18}$$

Table 7 summarizes these equations. For the data in order HEG+1, chips S4 and S5 were combined because of the two chips have similar efficiencies and there were not enough data for each chip to get an accurate fit. These fits give the first order correction for grade migration that is dependent only on count rate.

Order	Chip(s)	Correction Equation	Uncertainty
MEG+1	S3	$1.001 + 5.929\times10^{-4}\times$R	4.927×10^{-2}
MEG+1	S4	$0.978 + 3.020\times10^{-4}\times$R	3.187×10^{-2}
MEG-1	S2	$0.977 + 3.228\times10^{-4}\times$R	3.574×10^{-2}
MEG-1	S3	$1.078 + 7.559\times10^{-4}\times$R	5.864×10^{-2}
HEG+1	S3	$0.963 + 5.358\times10^{-4}\times$R	4.434×10^{-2}
HEG+1	S4,S5	$0.983 + 2.513\times10^{-4}\times$R	4.147×10^{-2}
HEG-1	S1	$1.043 + 7.360\times10^{-4}\times$R	4.261×10^{-2}
HEG-1	S2	$0.987 + 1.086\times10^{-4}\times$R	4.142×10^{-2}

Table 7. Summary of branching ratio correction count rate, where "count rate" is the average counts/cm^2/s, within the extraction ring of the dispersed spectrum.

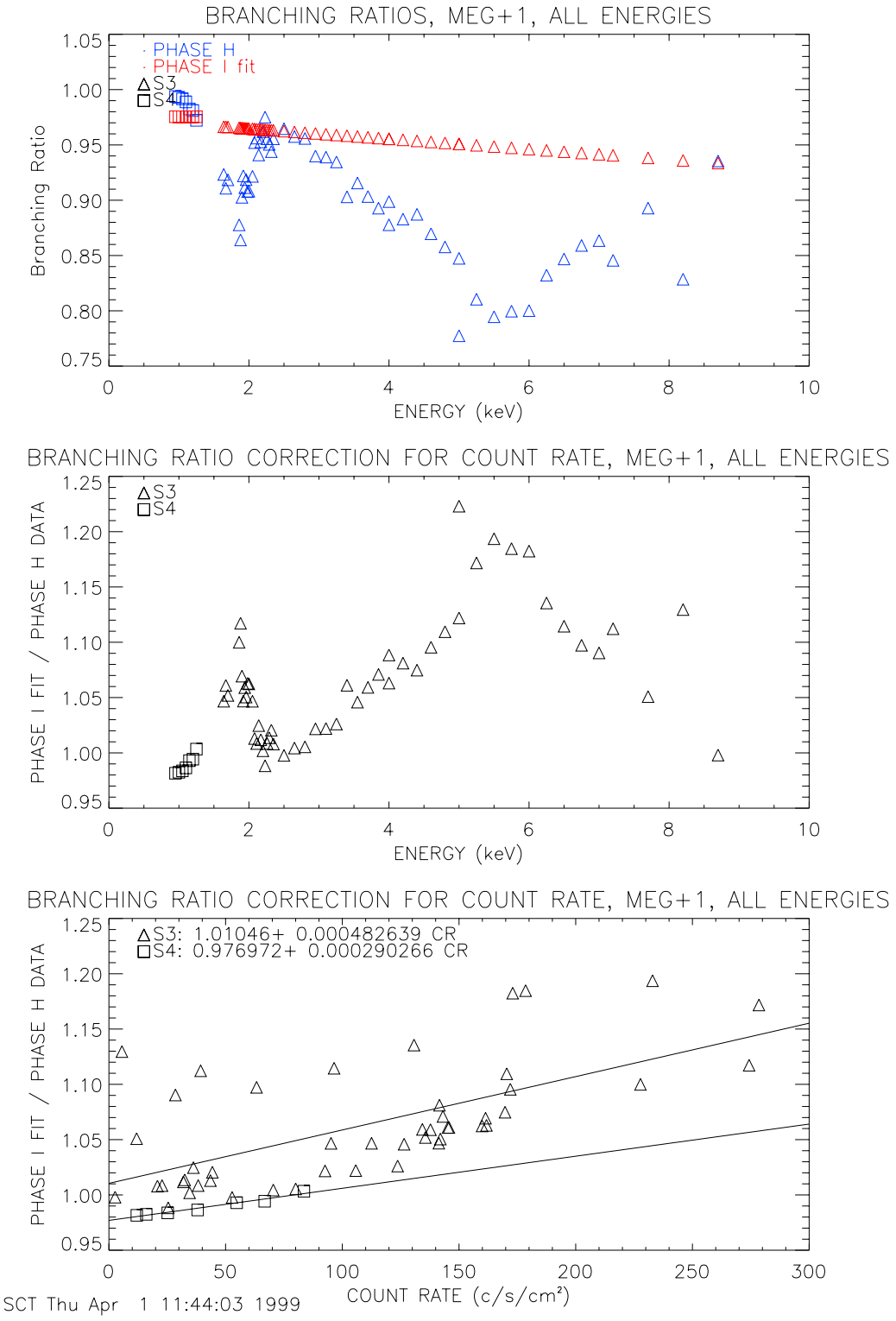

Figure 23. Plot of branching ratios and count rate corrections for order MEG+1.

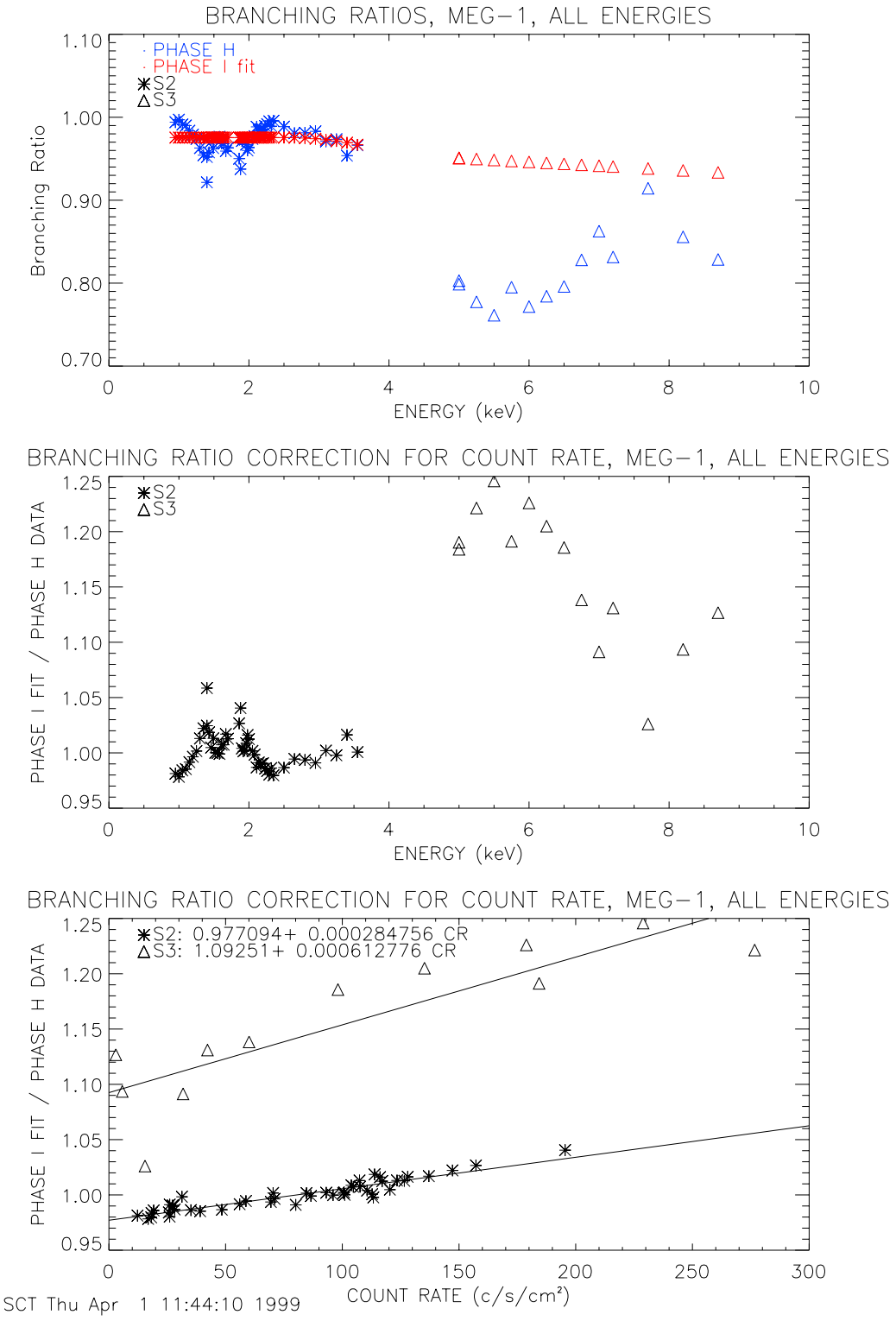

Figure 24. Plot of branching ratios and count rate corrections for order MEG-1.

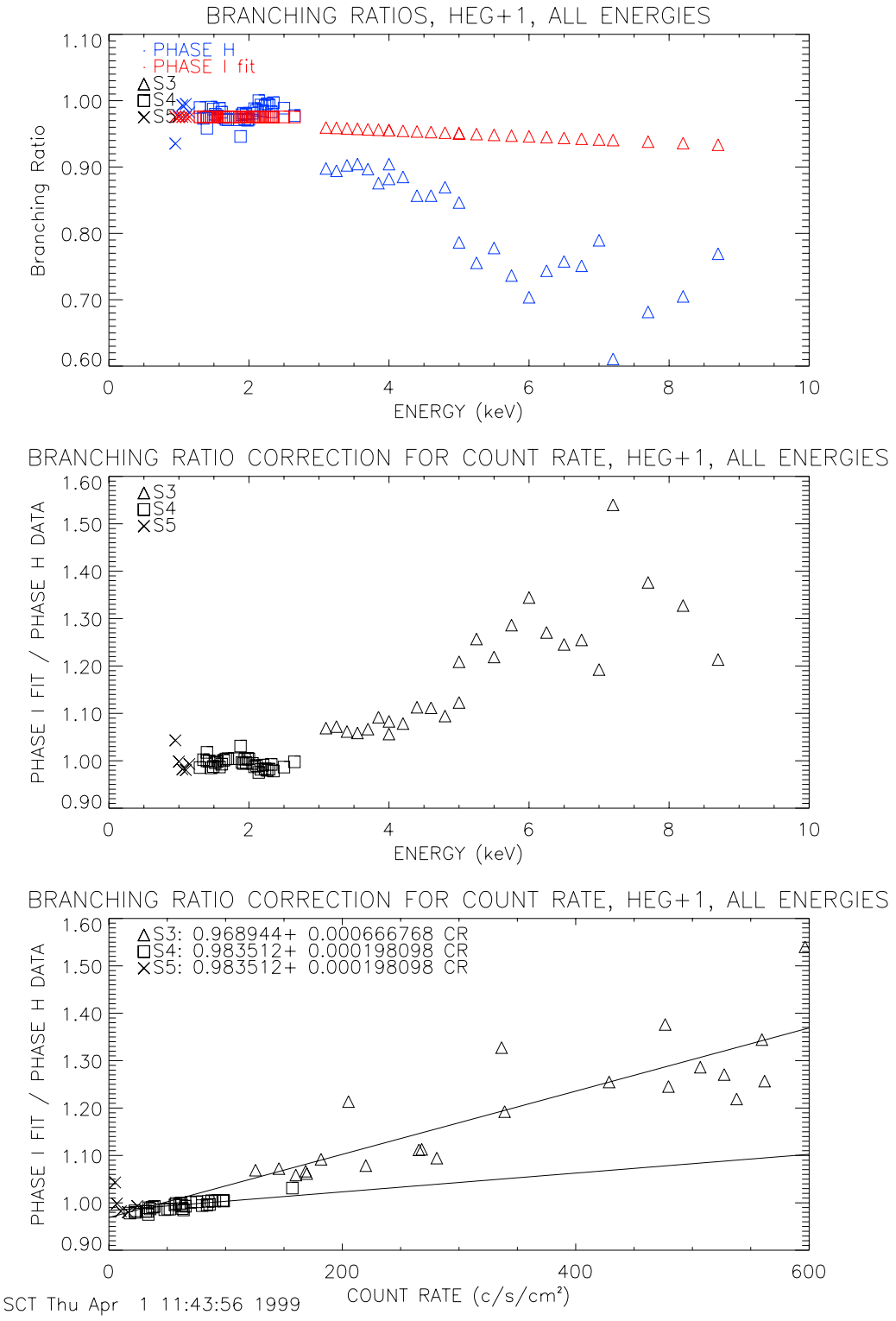

Figure 25. Plot of branching ratios and count rate corrections for order HEG+1.

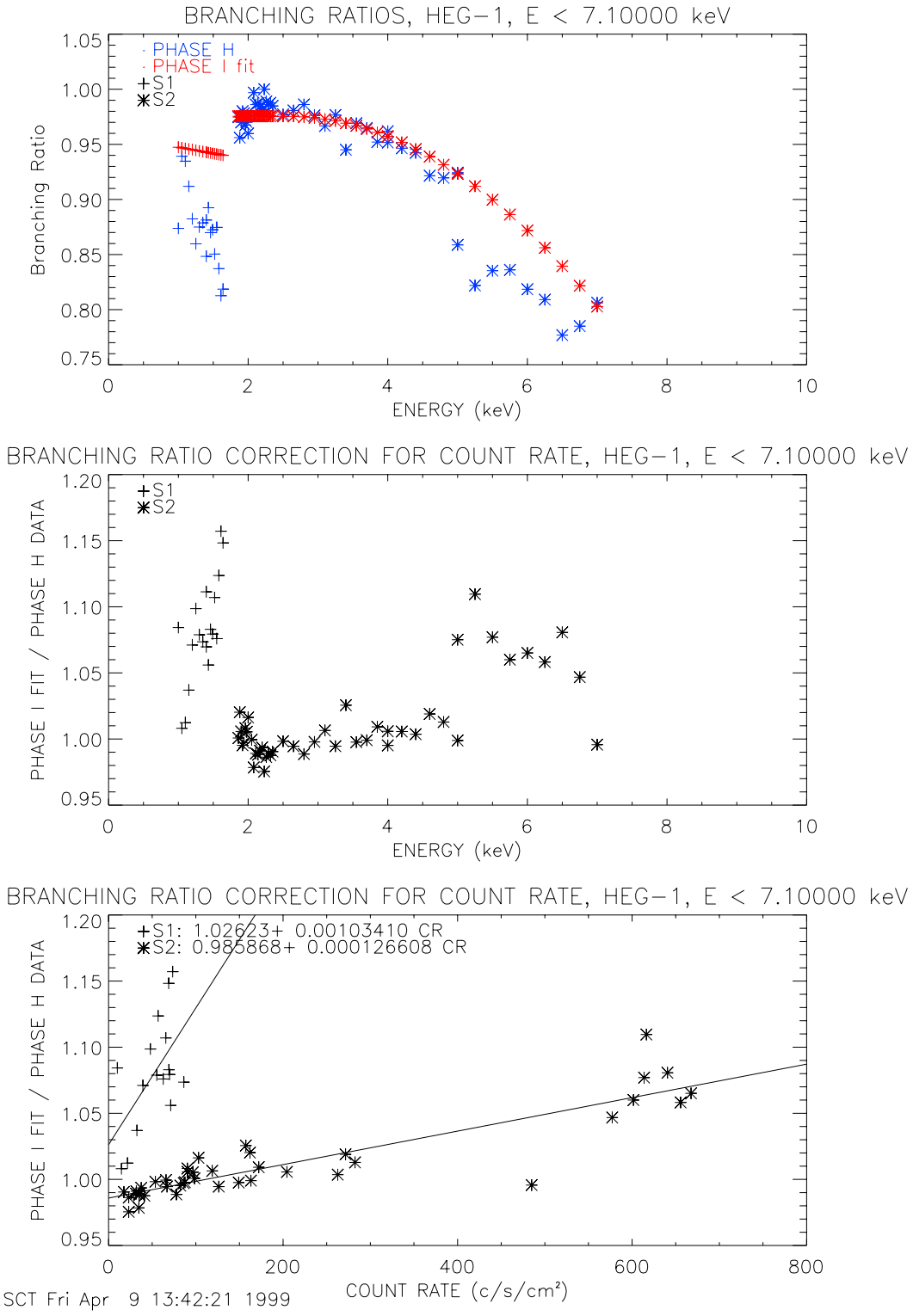

Figure 26. Plot of branching ratios and count rate corrections for order HEG-1.

6.3. Effective Areas After Grade Migration Correction

Grade migration was observed in the data with the highest count rates and for energies above 4 keV, where there were only DCM data available. Figures 27 and 28 show the MEG and HEG $\pm 1^{st}$ order comparison between the measured and modeled absolute effective area before and after the correction factors for grade migration have been applied. The top plots show the data with no correction, the middle show the data with the correction obtained from sub-assembly data (listed in Tables 4 and 5), and the bottom show the correction based on the phase I data. The equations for the phase I based corrections are listed in Table 7.

In this energy range, the MEG average count rate is around 300 counts/cm^2/s, which is much closer to the sub-assembly and phase I count rates, and therefore only a small effect on grade migration due to count rate is expected. The correction is usually less than 20%. For MEG-1, there is no corrected data between 4 and 5 keV, where the defocused lines span two different chips. Both types of corrections result in a match with the model for all other data for the MEG.

The count rates in the HEG data are about around 600 counts/cm^2/s and clear evidence of a count rate induced change in grade migration is visible. After the simpler sub-assembly based correction, the data still fall short for the HEG for most energies. With the phase I based correction, for HEG+1, where the data are on S3, a BI device, the correction in the data (as much as 50%) resulted in a match with the model. However, this correction was not enough for HEG-1, where the data are on S2, a FI device. Unfortunately, we do not have any more high count rate data at high energies on a FI chip to engage in a more deep investigation, but from all the evidence so far we have no indication that there is an asymmetry in the HEG efficiencies concerning the sign of the orders (see the 1998 SPIE paper by Flanagan[10]). Thus it is likely that we look at a divergence in behavior at higher count rates in BI and FI CCD devices. A similar effect has been pointed out in the ACIS effective area report by Allen,[2] where especially for the investigated FI devices counts were lost at high energies and count rates due to the ineffectivity of the event detection algorithm.

It should also be noted that the count rates given for the DCM data are average count rates over the area of the extraction ring. Therefore, localized count rates within that ring can be both lower and higher than this value. This adds another source of uncertainty to this correction.

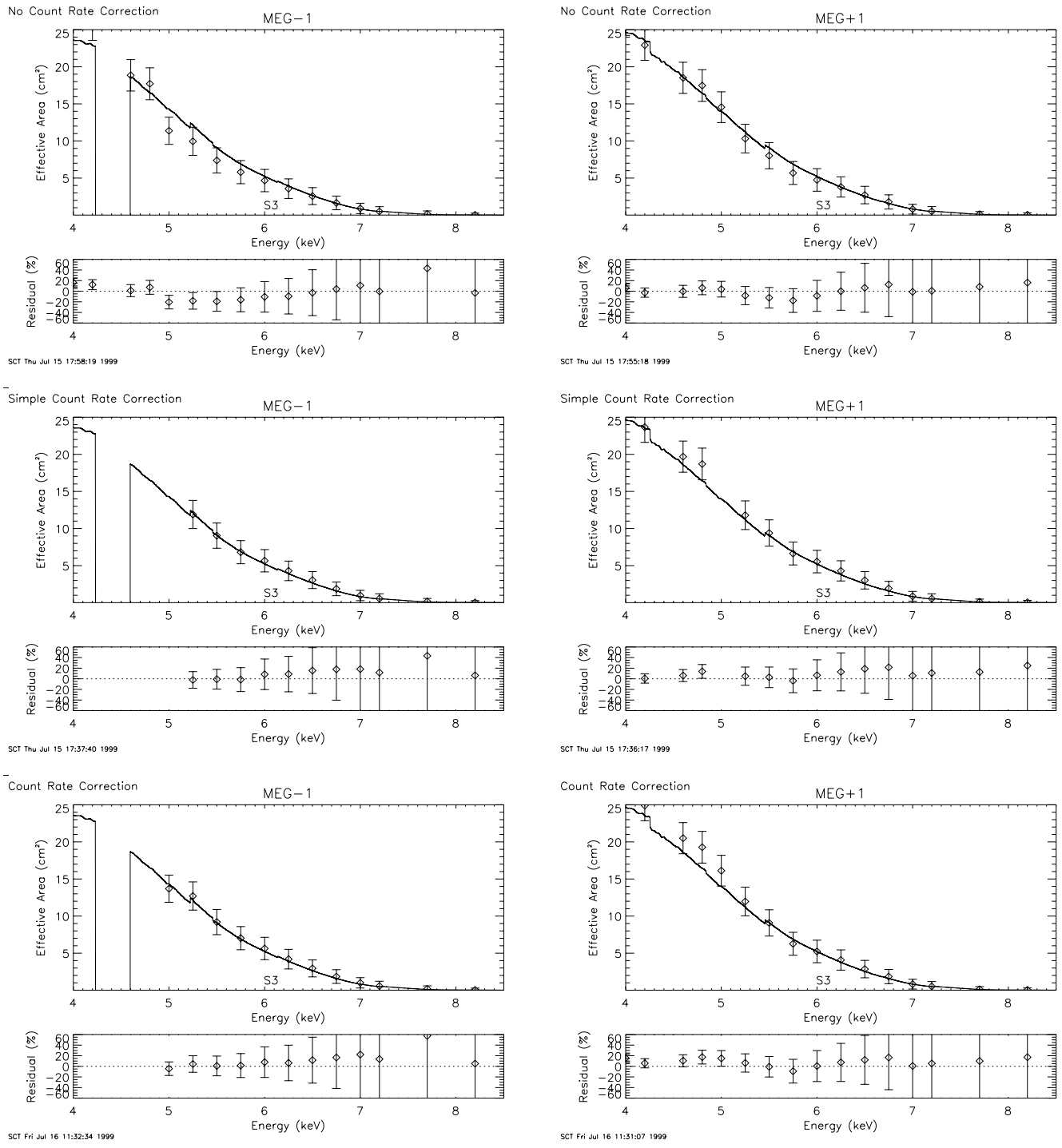

Figure 27. Comparison of measured absolute effective areas at XRCF of the MEG 1^{st} order to the modeled effective area before and after the grade migration correction factors have been applied. The top plots show the uncorrected data. The middle plots show the data corrected using the ratio the BR from phase H to sub-assembly. The bottom plots show a the data after a count rate base correction obtained from phase I data has been applied. Included under each plot is the residual from the model, in percent.

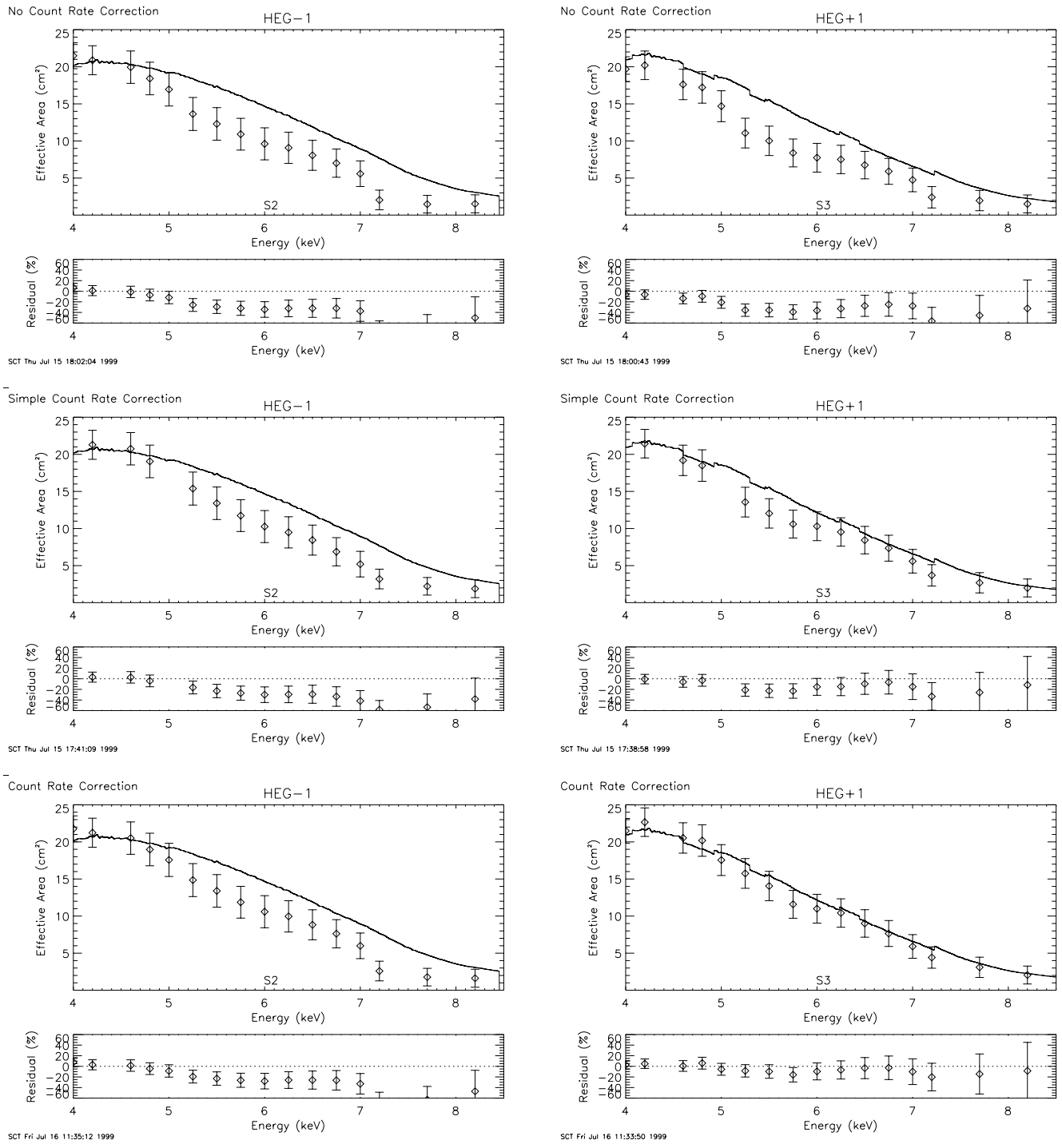

Figure 28. Comparison of measured absolute effective areas at XRCF of the HEG 1^{st} order to the modeled effective area before and after the grade migration correction factors have been applied. The top plots show the uncorrected data. The middle plots show the data corrected using the ratio the BR from phase H to sub-assembly. The bottom plots show a the data after a count rate base correction obtained from phase I data has been applied. Included under each plot is the residual from the model, in percent.

7. CONCLUSIONS

We analyzed effective area measurements performed at XRCF with the HETGS, by using the DCM energy scans in the energy range from 950 eV to 8700 eV, EIPS measurements in the energy range of 525 eV to 1740 eV, and HiREFS measurements in the energy range of 486 to 800 eV. The measurements were designed to produce sufficient flux in the 1^{st} and higher orders, therefore the 0^{th} order measurements were dominated by pile-up effects. Tables 8 through 12 summarize the measured effective areas for the DCM, EIPS, and HiREFS measurements, where the data has been corrected for all known effects mentioned in this paper, except for count rate induced grade migration. Tables 8 through 10 list the data from Figures 13 through 17, and Tables 11 and 12 list the data from Figures 18 and 19.

With higher count rates and energies, events will have a tendency to migrate into higher number grades. In Table 13, we give the results of performing a count rate dependent correction for this grade migration, for energies at and above 4.0 keV (as shown in Figures 27 and 28).

Our analysis resulted in the following conclusions:

• The absolute effective area of the combined 0^{th} order in MEG and HEG was measured to an accuracy per point better than 5% in with the DCM source the range 0.9 and 3.0 keV. The larger uncertainties were introduced by systematic errors from the DCM. At energies above 3 keV the measurements were entirely dominated by pile-up effects and the effective area in this range could only be verified with an uncertainty above 20%.

• The absolute effective areas of the 1^{st} orders were determined with an accuracy per point between 5 and 10% for the MEG and between 10 and 15% for the HEG over most of the energy range with the DCM source. Above ∼5 keV counting statistics degrades significantly.

• Although dominated by large statistical uncertainties the measured effective areas for the MEG 3^{rd} and the HEG 2^{nd} orders using DCM data agree very well with the expectation.

• With the EIPS, the effective areas for the MEG were determined with an accuracy per point of generally less than 10%, and less than 15% for the HEG, which are largely driven by the more extensive analysis that was required. The 1^{st} order HiREFS measurements were determined with an accuracy per point of less than 10% for MEG and HEG 1^{st} orders. The 2^{nd} order HiREFS measurements had large uncertainties driven by the uncertainty in the BND fit. These points are included only for completeness.

• The measured areas in the 1^{st} orders for the MEG and HEG match the expectation from the XRCF HRMA measurements combined with the sub-assembly results for the ACIS-S and the HETG to quite a high degree for all 3 sources. The HEG measurements above 4 keV are affected by count rate induced effects in the CCD devices, which were identified by Allen *et al.*[2] as higher order pile-up effects due to grade migration and lost charge effects.

• The only exception to this is for MEG 1^{st} orders below 1.5 keV. Here, the measured effective area falls short of the expectation by ∼20%. Because this is seen using 3 separate sources and is not seen in the HEG, we suspect that the MEG efficiency is overestimated in this region.

• An updated version of the MEG and HEG grating efficiencies is expected to be released in the near future. It will contain as much as a -10% correction below 1 keV for MEG 1^{st} orders, and as much as a +20% correction below 2 keV for HEG 1^{st} orders.

• When correcting the measured effective area for grade migration using the method suggested by Allen *et al.*,[1] MEG $\pm 1^{st}$ orders match the expectation quite well, but HEG $\pm 1^{st}$ orders still fall short of the expectation. When using phase I data to correct for grade migration, the measured effective area matches the expectation for MEG $\pm 1^{st}$ and HEG $+1^{st}$ orders, which fall on a BI device, but still falls short for HEG -1^{st} order, where the data fall on a FI device. Because none of the data collected for the HETG suggest that there are asymmetries in the HEG $\pm 1^{st}$ orders, this difference is likely to be a result of data falling on different types of CCDs.

Energy eV	0^{th} cm^2	MEG 1 cm^2	MEG-1 cm^2	MEG 3 cm^2	MEG-3 cm^2	HEG 1 cm^2	HEG-1 cm^2	HEG 2 cm^2	HEG-2 cm^2
950	51.6±2.4	14.6±1.1	15.3±1.2	-	-	4.0±0.6	5.5±0.7	-	-
	51.5	18.6	19.9	0.0	0.0	4.0	4.1	0.0	0.0
1000	54.1±2.6	18.4±1.3	19.4±1.4	-	0.9±0.3	4.9±0.7	6.5±0.8	-	-
	54.7	22.6	23.9	0.0	0.0	4.8	7.2	0.0	0.0
1050	55.1±2.8	22.6±1.7	23.0±1.7	-	2.3±0.5	5.7±0.8	7.8±1.0	-	-
	57.1	27.2	28.6	0.0	2.7	5.7	8.0	0.0	0.0
1100	59.1±3.2	26.7±2.0	27.5±2.1	-	2.8±0.7	7.1±1.0	9.0±1.2	-	-
	57.5	32.1	33.5	0.0	3.2	6.7	9.1	0.0	0.0
1150	53.5±3.4	32.4±2.4	33.6±2.5	0.1±0.1	3.2±0.8	8.9±1.3	11.3±1.4	-	-
	56.9	37.4	38.9	0.0	3.7	8.0	10.4	0.0	0.0
1200	50.8±3.4	38.8±2.7	41.5±2.8	2.9±0.7	3.9±0.8	11.9±1.5	12.6±1.5	-	-
	56.1	43.4	44.9	4.3	4.4	9.5	11.5	0.0	0.0
1250	39.9±3.4	37.2±3.0	37.5±3.0	3.9±1.0	3.8±1.0	12.6±1.8	11.6±1.7	-	-
	54.6	48.6	50.2	4.8	4.9	11.4	13.9	0.0	0.0
1300	57.6±3.6	49.9±3.5	48.2±3.4	4.9±1.1	5.0±1.1	13.6±1.8	13.5±1.8	-	-
	53.0	53.8	55.3	5.3	5.3	13.2	16.2	0.0	0.0
1350	45.1±3.9	53.4±4.3	45.7±4.0	4.6±1.3	4.7±1.3	14.6±2.3	14.9±2.3	-	2.0±0.8
	51.8	58.9	60.5	5.8	5.8	15.3	18.5	0.0	2.5
1400	31.8±4.6	65.0±4.6	61.1±4.4	6.3±1.4	5.7±1.4	21.3±2.6	21.4±2.6	-	3.3±1.0
	51.0	63.7	65.2	6.2	6.3	17.7	21.5	0.0	2.7
1430	39.8±3.3	61.8±3.7	55.1±3.5	5.4±1.1	5.2±1.1	18.9±2.1	19.8±2.1	-	3.0±0.8
	51.1	16.9	67.9	6.5	3.2	19.2	22.4	0.0	2.8
1460	38.6±3.2	57.3±3.7	55.3±3.6	5.1±1.1	4.8±1.1	18.9±2.1	17.9±2.1	-	2.6±0.8
	51.3	78.0	70.0	6.6	8.1	20.4	23.5	0.0	2.8
1490	59.5±3.4	68.3±3.8	64.1±3.7	6.2±1.2	5.1±1.0	21.0±2.1	20.6±2.1	-	2.9±0.8
	52.0	79.8	72.2	6.8	8.0	21.9	25.7	0.0	2.9
1520	57.8±3.1	76.8±3.5	70.6±3.3	6.6±1.0	6.2±1.0	24.3±2.0	24.8±2.0	-	3.3±0.7
	52.7	81.0	74.7	7.1	8.4	23.5	27.1	0.8	3.0
1550	54.2±3.0	77.1±3.5	65.6±3.2	6.4±1.0	6.4±1.0	24.2±2.0	23.8±1.9	0.3±0.2	3.2±0.7
	52.2	83.3	77.3	7.3	8.6	25.3	28.6	1.8	3.1
1580	46.8±2.9	76.6±3.5	61.6±3.1	5.9±1.0	6.3±1.0	24.2±2.0	22.0±1.9	2.0±0.6	3.0±0.7
	50.8	75.9	67.6	6.4	7.6	23.0	25.8	2.7	2.7
1610	47.2±3.1	75.0±3.8	60.3±3.4	6.2±1.1	6.4±1.1	24.2±2.2	21.9±2.1	3.0±0.8	3.3±0.8
	52.9	76.2	68.6	6.4	7.6	24.2	26.6	2.7	2.7
1640	48.8±3.1	68.2±3.6	61.5±3.4	5.9±1.1	5.9±1.1	24.8±2.2	25.8±2.2	3.1±0.8	3.0±0.8
	55.7	76.5	69.4	6.5	7.5	25.3	27.4	2.7	2.8
1670	52.0±3.6	64.1±3.8	64.4±3.9	6.2±1.2	6.3±1.2	26.4±2.5	24.2±2.4	3.1±0.8	3.2±0.9
	59.7	79.7	71.4	6.7	7.5	26.9	27.8	2.8	2.8
1700	46.2±3.5	55.1±3.7	54.8±3.7	5.2±1.1	5.3±1.2	23.4±2.4	23.2±2.4	2.8±0.8	2.6±0.8
	64.2	80.1	72.3	6.7	7.7	28.3	29.7	2.9	2.9
1860	77.1±4.9	43.2±4.7	32.4±4.0	2.6±1.1	3.9±1.4	12.9±2.6	13.1±2.6	1.1±0.8	1.1±0.8
	92.8	74.6	48.4	3.7	7.3	21.6	22.4	1.8	1.9
1880	62.8±5.8	59.0±5.1	46.9±4.5	3.6±1.3	5.7±1.6	23.4±3.2	24.0±3.3	2.1±1.0	2.0±0.9
	96.7	72.6	52.6	4.8	7.1	24.3	24.9	2.0	2.1
1900	79.7±4.8	62.4±4.0	46.0±3.4	3.0±0.9	5.3±1.2	22.2±2.4	23.1±2.4	2.0±0.7	1.9±0.7
	96.7	71.4	50.5	4.6	6.9	23.7	24.2	2.0	2.0

Table 8. Table of results of measured versus predicted effective areas of the HETGS with the DCM. The stated uncertainties include only counting statistics and BND uncertainties. The second row for each energy lists the modeled effective area from the HRMA XRCF model and the ACIS and HETG sub-assembly predictions. (part 1 of 3)

Energy eV	0^{th} cm^2	MEG 1 cm^2	MEG-1 cm^2	MEG 3 cm^2	MEG-3 cm^2	HEG 1 cm^2	HEG-1 cm^2	HEG 2 cm^2	HEG-2 cm^2
1920	99.6±4.9	66.6±3.8	49.9±3.3	3.9±0.9	6.1±1.1	24.4±2.3	25.4±2.3	2.0±0.7	2.0±0.7
	101.2	71.0	52.2	4.7	6.9	24.7	25.4	2.0	0.8
1940	95.9±4.9	63.5±3.7	49.5±3.3	3.8±0.9	5.9±1.1	25.5±2.3	26.3±2.4	2.4±0.7	2.1±0.7
	104.9	69.3	51.0	4.6	7.1	24.7	25.4	2.0	2.9
1960	106.9±5.2	62.7±3.8	48.1±3.3	4.3±1.0	5.2±1.1	24.2±2.3	25.4±2.4	2.3±0.7	1.9±0.7
	110.2	68.4	50.7	4.6	6.7	25.1	25.7	2.0	2.8
1980	109.4±5.5	63.5±4.0	48.0±3.5	4.6±1.1	5.3±1.2	24.8±2.5	24.9±2.5	2.0±0.7	2.5±0.8
	115.5	67.1	50.4	4.5	6.6	25.5	26.1	2.0	2.8
2000	104.9±5.5	55.6±4.0	43.4±3.5	3.9±1.1	5.0±1.2	22.3±2.5	23.0±2.6	1.8±0.7	2.2±0.8
	119.5	64.8	49.3	4.4	6.2	25.5	26.1	2.0	2.8
2050	91.9±4.5	43.6±3.1	33.8±2.7	3.2±0.8	3.9±0.9	18.5±2.0	19.3±2.0	1.5±0.6	1.8±0.6
	117.7	51.8	40.9	3.7	5.3	23.4	23.9	1.8	2.5
2080	91.3±3.8	32.8±2.1	24.0±1.8	1.7±0.5	2.1±0.5	16.4±1.5	16.1±1.5	1.3±0.4	1.2±0.4
	75.4	28.8	23.1	2.1	2.9	16.4	16.7	1.2	1.7
2110	90.8±4.0	29.7±2.0	23.1±1.8	2.1±0.5	2.3±0.6	16.0±1.5	16.9±1.5	1.7±0.5	2.0±0.5
	84.2	28.4	23.0	2.0	2.8	16.4	16.7	1.2	1.7
2140	98.9±4.0	29.6±2.0	21.8±1.7	1.8±0.5	2.0±0.5	16.7±1.5	17.4±1.5	1.1±0.4	1.6±0.5
	83.6	24.2	19.8	1.8	2.5	15.1	15.3	1.1	1.4
2170	96.7±4.2	23.7±1.9	20.7±1.7	1.2±0.4	1.5±0.5	15.1±1.5	13.9±1.4	0.8±0.4	1.5±0.5
	88.0	21.8	17.5	1.5	2.1	13.9	14.1	1.0	1.3
2200	102.1±4.8	22.2±1.9	17.9±1.7	1.4±0.5	1.6±0.5	14.2±1.5	14.4±1.6	0.9±0.4	0.9±0.4
	107.2	20.8	16.8	1.5	2.0	13.4	13.6	0.9	1.2
2230	135.8±5.0	18.2±1.7	14.1±1.5	1.0±0.4	1.1±0.4	9.2±1.2	9.5±1.2	0.8±0.4	0.7±0.3
	127.0	16.1	13.1	1.1	1.5	10.5	10.7	0.7	1.0
2260	114.3±4.6	15.5±1.6	13.1±1.4	1.0±0.4	1.3±0.4	9.2±1.2	9.7±1.2	0.8±0.4	0.8±0.3
	98.9	14.5	11.9	1.0	1.3	8.8	8.9	0.7	0.9
2290	78.8±4.8	15.1±1.9	12.6±1.7	1.1±0.5	1.2±0.5	8.8±1.4	8.5±1.4	0.7±0.4	0.8±0.4
	95.9	16.2	13.4	1.1	1.5	9.5	9.6	0.7	1.0
2320	107.3±5.6	19.1±2.2	16.1±2.0	1.4±0.6	1.6±0.6	9.9±1.5	10.9±1.6	1.0±0.5	1.1±0.5
	98.5	14.9	12.1	1.0	1.3	8.7	8.8	0.7	0.9
2350	92.6±4.0	15.6±1.5	14.3±1.5	0.9±0.4	1.2±0.4	7.9±1.1	7.8±1.1	0.6±0.3	0.8±0.3
	84.0	16.3	13.3	1.1	1.5	8.9	9.1	0.7	1.0
2500	70.5±3.1	20.8±1.6	18.8±1.5	1.7±0.4	1.6±0.4	12.2±1.2	12.6±1.2	0.6±0.3	1.0±0.3
	75.1	20.2	17.3	1.5	1.8	11.2	11.3	1.0	1.2
2650	80.9±3.4	22.7±1.8	18.8±1.6	1.6±0.5	1.4±0.4	11.8±1.3	13.0±1.4	1.3±0.4	1.4±0.4
	77.8	21.0	18.3	1.6	1.6	12.2	12.4	1.0	1.2
2800	82.7±3.7	22.5±1.9	20.1±1.8	1.8±0.5	1.8±0.5	13.0±1.4	13.6±1.5	1.0±0.4	1.0±0.4
	80.4	22.0	19.5	1.7	1.7	12.8	12.9	1.1	1.3
2950	85.7±3.9	24.4±2.0	21.7±1.9	1.9±0.6	2.0±0.6	17.5±1.7	14.5±1.6	1.2±0.5	0.8±0.4
	81.3	22.6	20.9	1.8	1.8	15.6	14.3	1.2	1.4
3100	102.2±4.3	25.4±2.2	23.1±2.1	2.4±0.7	2.2±0.6	17.8±1.8	17.9±1.8	1.3±0.5	1.3±0.5
	88.6	23.7	22.2	1.9	1.9	16.7	15.7	1.3	1.4
3250	94.7±4.7	25.1±2.3	24.3±2.3	2.1±0.7	2.3±0.7	17.4±1.9	16.6±1.9	1.4±0.6	1.1±0.5
	92.6	24.4	22.5	2.0	2.0	17.4	16.3	1.3	1.4

Table 9. Table of results of measured versus predicted effective areas of the HETGS with the DCM. The stated uncertainties include only counting statistics and BND uncertainties. The second row for each energy lists the modeled effective area from the HRMA XRCF model and the ACIS and HETG sub-assembly predictions. (part 2 of 3)

Energy eV	0^{th} cm^2	MEG 1 cm^2	MEG-1 cm^2	MEG 3 cm^2	MEG-3 cm^2	HEG 1 cm^2	HEG-1 cm^2	HEG 2 cm^2	HEG-2 cm^2
3400	109.3±5.3	26.3±2.5	25.2±2.4	2.4±0.8	2.3±0.7	18.6±2.1	18.9±2.1	1.5±0.6	0.9±0.5
	105.7	24.4	23.2	2.0	2.0	19.2	17.3	1.4	1.3
3550	111.3±5.1	25.2±2.4	28.1±2.5	2.2±0.7	2.4±0.7	19.3±2.1	19.5±2.1	1.3±0.5	1.2±0.5
	112.5	25.8	24.0	2.1	2.1	19.1	18.5	1.4	1.4
3700	122.8±5.4	25.4±2.4	24.7±2.4	2.4±0.7	2.4±0.7	19.5±2.1	20.5±2.2	1.8±0.6	1.4±0.6
	121.8	25.9	24.3	2.1	2.1	21.0	19.3	1.4	1.4
3850	125.9±5.9	24.4±2.5	27.3±2.7	2.2±0.8	2.3±0.8	18.4±2.2	19.5±2.3	1.3±0.6	1.5±0.6
	129.1	25.4	24.1	2.1	2.1	20.7	19.8	1.4	1.4
4000	81.2±4.5	26.2±1.9	27.4±2.0	2.2±0.6	2.3±0.6	19.7±1.7	21.5±1.7	1.5±0.5	1.7±0.5
	136.4	24.6	23.6	2.1	2.1	20.9	20.2	1.4	1.4
4200	148.0±5.5	22.9±2.0	25.7±2.2	1.4±0.5	2.1±0.6	20.2±1.9	20.9±2.0	1.4±0.5	1.6±0.5
	146.5	23.5	22.9	2.0	2.0	21.6	20.6	1.4	1.4
4400	155.3±6.1	-	-	-	-	-	-	-	-
	153.7	20.7	9.3	1.9	1.9	21.3	20.7	1.4	1.4
4600	153.2±6.2	18.5±2.1	18.9±2.1	1.8±0.7	1.9±0.7	17.6±2.0	19.9±2.2	1.4±0.6	1.6±0.6
	155.6	18.5	18.6	1.7	1.7	20.4	20.2	1.3	1.4
4800	155.1±6.5	17.5±2.1	17.7±2.2	1.5±0.6	2.0±0.7	17.2±2.1	18.4±2.2	1.2±0.6	1.3±0.6
	156.3	16.4	16.5	1.5	1.6	19.0	19.8	1.3	1.3
5000	131.7±6.4	14.6±2.1	11.4±1.8	1.4±0.6	1.5±0.7	14.7±2.1	16.9±2.2	1.0±0.5	1.1±0.6
	154.2	14.0	14.3	1.4	1.4	18.6	19.2	1.2	1.2
5250	151.3±7.4	10.3±1.9	10.0±1.9	1.0±0.6	1.5±0.7	11.1±2.0	13.6±2.2	1.2±0.7	1.1±0.6
	146.8	11.3	12.2	1.0	1.2	17.2	18.4	1.2	1.2
5500	142.5±7.4	8.0±1.8	7.4±1.7	0.9±0.6	1.0±0.6	10.0±2.0	12.3±2.2	1.0±0.6	1.0±0.6
	136.8	9.2	9.1	0.8	0.9	15.6	17.4	1.1	1.1
5750	116.2±6.8	5.7±1.5	5.8±1.6	0.7±0.5	0.8±0.6	8.4±1.9	10.9±2.1	0.4±0.4	0.9±0.6
	124.4	6.9	6.9	0.6	0.7	13.8	16.1	0.5	1.0
6000	114.0±7.2	4.7±1.5	4.7±1.5	0.5±0.5	0.6±0.5	7.7±1.9	9.6±2.2	0.6±0.5	0.8±0.6
	112.4	5.2	5.2	0.5	0.6	12.2	14.7	0.8	0.9
6250	71.9±5.7	3.8±1.4	3.6±1.3	0.4±0.4	0.5±0.5	7.5±1.9	9.1±2.1	0.5±0.5	0.8±0.6
	101.4	3.8	3.9	0.3	0.4	11.2	13.4	0.6	0.8
6500	69.0±5.7	2.7±1.2	2.6±1.1	0.2±0.3	0.4±0.5	6.7±1.9	8.1±2.0	0.4±0.4	0.7±0.6
	87.6	2.5	2.6	0.2	0.3	9.3	11.9	0.6	0.7
6750	59.7±5.4	1.8±1.0	1.7±0.9	0.2±0.3	0.2±0.3	5.9±1.7	7.0±1.9	0.4±0.5	0.6±0.6
	73.2	1.6	1.6	0.1	0.2	7.9	10.3	0.5	0.6
7000	46.5±4.7	0.8±0.7	0.9±0.7	0.1±0.2	0.1±0.2	4.8±1.6	5.6±1.7	0.3±0.4	0.5±0.5
	60.5	0.8	0.8	0.1	0.1	6.6	8.9	0.4	0.5
7200	33.2±5.1	0.5±0.7	0.5±0.7	0.0±0.2	0.1±0.2	2.4±1.4	2.0±1.3	0.3±0.5	0.4±0.6
	51.7	0.5	0.5	0.0	0.1	5.5	7.7	0.3	0.4
7700	25.6±4.7	0.1±0.4	0.2±0.4	0.0±0.1	0.0±0.1	2.0±1.4	1.5±1.2	0.2±0.4	0.3±0.5
	37.0	0.1	0.1	0.0	0.0	3.6	4.8	0.2	0.3
8200	13.0±3.3	0.1±0.3	0.0±0.2	0.0±0.1	0.0±0.1	1.5±1.2	1.5±1.2	0.1±0.3	0.2±0.4
	25.7	0.0	0.0	0.0	0.0	2.2	3.1	0.1	0.2
8700	3.0±1.4	0.0±0.2	0.0±0.2	0.0±0.1	0.0±0.1	1.2±1.0	1.3±1.0	0.1±0.2	0.1±0.3
	19.4	0.0	0.0	0.0	0.0	1.4	0.4	0.1	0.1

Table 10. Table of results of measured versus predicted effective areas of the HETGS with the DCM. The stated uncertainties include only counting statistics and BND uncertainties. The second row for each energy lists the modeled effective area from the HRMA XRCF model and the ACIS and HETG sub-assembly predictions. (part 3 of 3)

TRW-ID H-HAS-EA-	Line	Energy eV	MEG 1 cm^2	MEG -1 cm^2	HEG 1 cm^2	HEG -1 cm^2
2.001	AlKα	1487	58.2 ± 5.4 79.5	57.5 ± 5.2 71.8	20.6 ± 1.9 21.7	20.4 ± 1.9 25.5
6.001	OKα	524	1.8 ± 0.3 2.0	5.5 ± 0.8 6.2	- 0.0	- 0.0
6.002	FeLα	705	3.1 ± 0.5 4.9	8.4 ± 1.3 11.4	- 0.0	- 1.0
6.002	FeLl	615	1.3 ± 0.2 0.0	4.9 ± 0.7 6.9	- 0.0	- 0.0
6.002	OKα	524	1.6 ± 1.0 2.0	3.3 ± 0.9 6.2	- 0.0	- 0.0
6.003	CuLα	929	13.8 ± 1.2 16.7	14.9 ± 2.3 17.9	3.6 ± 0.3 3.6	3.6 ± 0.6 3.7
6.003	CuLζ	811	10.2 ± 4.1 9.5	17.7 ± 6.5 17.1	1.5 ± 0.5 2.0	1.3 ± 0.4 2.1
6.004	SiKα	1740	69.5 ± 10.2 78.3	67.3 ± 11.6 72.6	26.9 ± 3.4 29.7	24.8 ± 2.9 0.0

Table 11. Table of results of measured versus predicted effective areas for EIPS measurements. The second row for each energy lists the modeled effective area from the HRMA XRCF model and the ACIS and HETG sub-assembly predictions.

TRW-ID H-HAS-EA-	HiREFS Order	Energy eV	MEG 1 cm^2	MEG -1 cm^2	HEG 1 cm^2	HEG -1 cm^2
10.001	2^{nd} of 392 eV	784	9.2 ± 17.1 8.3	18.4 ± 34.3 16.1	- 0.0	2.3 ± 4.3 1.8
10.002	1^{st}	486	1.4 ± 0.2 1.1	5.0 ± 0.7 4.4	- 0.0	- 0.0
10.002	2^{nd} of 486 eV	972	19.9 ± 3.4 20.3	23.0 ± 4.0 21.6	5.0 ± 0.9 4.4	6.8 ± 1.2 6.8
10.003	1^{st}	577	1.0 ± 0.1 1.0	4.8 ± 0.4 4.5	- 0.0	- 0.0
10.004	1^{st}	642	2.3 ± 0.2 2.7	7.3 ± 0.5 8.3	- 0.0	- 0.0
10.005	1^{st}	751	5.2 ± 0.3 6.8	11.2 ± 0.6 13.8	- 0.0	1.1 ± 0.1 1.4
10.006	1^{st}	799	6.7 ± 0.4 8.9	14.1 ± 0.9 16.8	1.4 ± 0.1 1.9	1.6 ± 0.1 1.9

Table 12. Table of results of measured versus predicted effective areas for HiREFS measurements. The second row for each energy lists the modeled effective area from the HRMA XRCF model and the ACIS and HETG sub-assembly predictions.

Energy eV	MEG 1 cm^2	MEG-1 cm^2	HEG 1 cm^2	HEG-1 cm^2
4000	28.5±1.9	0.0±2.0	21.5±1.7	21.8±1.7
	24.6	23.6	20.9	20.2
4200	24.9±2.0	0.0±2.2	22.7±1.9	21.2±2.0
	23.5	22.9	21.6	20.6
4600	20.5±2.1	0.0±2.1	20.5±2.0	20.5±2.2
	18.5	18.6	20.4	20.2
4800	19.3±2.1	0.0±2.2	20.2±2.1	19.0±2.2
	16.4	16.5	19.0	19.8
5000	16.1±2.1	13.7±1.8	17.5±2.1	17.6±2.2
	14.0	14.3	18.6	19.2
5250	12.0±1.9	12.7±1.9	15.7±2.0	14.9±2.2
	11.3	12.2	17.2	18.4
5500	9.1±1.8	9.2±1.7	14.1±2.0	13.4±2.2
	9.2	9.1	15.6	17.4
5750	6.3±1.5	7.0±1.6	11.6±1.9	11.9±2.1
	6.9	6.9	13.8	16.1
6000	5.2±1.5	5.6±1.5	11.0±1.9	10.6±2.2
	5.2	5.2	12.2	14.7
6250	4.1±1.4	4.2±1.3	10.4±1.9	10.0±2.1
	3.8	3.9	11.2	13.4
6500	2.9±1.2	2.9±1.1	9.0±1.9	8.8±2.0
	2.5	2.6	9.3	11.9
6750	1.8±1.0	1.9±0.9	7.7±1.7	7.6±1.9
	1.6	1.6	7.9	10.3
7000	0.8±0.7	1.0±0.7	5.9±1.6	6.0±1.7
	0.8	0.8	6.6	8.9
7200	0.5±0.7	0.6±0.7	4.4±1.4	2.6±1.3
	0.5	0.5	5.5	7.7
7700	0.1±0.4	0.2±0.4	3.1±1.4	1.8±1.2
	0.1	0.1	3.6	4.8
8200	0.1±0.3	0.0±0.2	2.1±1.2	1.6±1.2
	0.0	0.0	2.2	3.1
8700	0.0±0.2	0.0±0.2	1.5±1.0	1.6±1.0
	0.0	0.0	1.4	0.4

Table 13. Table of results of measured versus predicted effective areas, MEG and HEG $\pm 1^{st}$ orders, of the HETGS with the DCM, after phase I count rate correction has been applied. The stated uncertainties are computed from counting statistics, BND uncertainties, and an uncertainty associated with the grade migration correction. The second row for each energy lists the modeled effective area from the HRMA XRCF model and the ACIS and HETG sub-assembly predictions.

REFERENCES

1. K. Allen, P.P. Plucinsky, B.R. McNamara, and R.J. Edgar, "A Study of the AXAF Effective Area with the ACIS Detector", A Memorandum from the AXAF Science Center, (February 1, 1999).
2. C.L. Allen, P.P. Plucinsky, B.R. McNamara, R.J. Edgar, N.S. Schulz, and J.W. Woo, "Analysis of the AXAF HRMA+ACIS effective area measurements from the XRCF" *X-Ray Optics, Instruments, and Missions*, Proc. SPIE, Vol. **3444**, (1998).
3. M.W. Bautz, F. Baganoff, T. Isobe, S.E. Jones, S.E. Kissel, B. LaMarr, H.L. Manning, M. Pivovaroff, G.Y. Prigozhin, J.A. Nousek, C.E. Grant, K. Nishikida, F. Scholze, R. Thornagel, and G. Ulm, "X-Ray CCD Calibration for the AXAF CCD Imaging Spectrometer", *X-Ray Optics, Instruments, and Missions*, Proc. SPIE, Vol. **3444**, (1998).
4. M. Bautz, J. Nousek, G. Garmire and the ACIS instrument team, "Science Instrument Calibration Report for the AXAF CCD Imaging Spectrometer (ACIS), Version 2.20", (1999).
5. M. Bautz, J. Nousek, G. Garmire and the ACIS instrument team, "Science Instrument Calibration Report for the AXAF CCD Imaging Spectrometer (ACIS)", available at *http://wwwastro.msfc.nasa.gov/xray/axafps.html* (1997).
6. J.E. Davis, H.L. Marshall, M.L. Schattenburg, and D. Dewey, "Analysis and Modeling of Anomalous Scattering in the AXAF HETGS", *X-Ray Optics, Instruments, and Missions*, Proc. SPIE, Vol. **3444**, (1998).
7. D. Dewey, D.N. Humpheries, G.Y. McLean and D.A. Moschella, "Laboratory Calibration of X-ray Transmission Diffraction Gratings", *EUX, X-Ray, and Gamma-Ray Instrumentation for Astronomy V*, Proc. SPIE, Vol. **2280**, 257-271 (1994).
8. D. Dewey, H.L. Marshall, K.A. Flanagan, C. Baluta, C.R. Canizares, D.S. Davis, J.E. Davis, T.T. Fang, D.P. Huenemoerder, J.H. Kastner, N.S. Schulz, M.W. Wise, J.J. Drake, J.Z. Juda, M. Juda, A.C. Brinkman, T. Gunsing, J. Kaastra, G. Hartner and P. Predehl, "Towards the Calibration of the HETG Effective Area", *Grazing Incidence and Multilayer X-Ray Optical Systems*, Proc. SPIE, Vol. **3113**, 144-159 (1997).
9. K.A. Flanagan, D. Dewey, L. Bordzol, "Calibration and Characterization of HETG grating elements at the MIT X-ray Grating Evaluation Facility", *SPIE Proceedings* **2518**, 438-456 (1995).
10. K.A. Flanagan, N.S. Schulz, G.D. Hartner, and P. Predehl, "HETG High-Order Diffraction Efficiency" *X-Ray Optics, Instruments, and Missions*, Proc. SPIE, Vol. **3444**, (1998).
11. J.J. Kolodziejczak, R.A. Austin, R.F. Elsner, M.K. Joy, M. Sulkanen, E.M. Kellogg, and B.J. Wargelin, "X-Ray Source System at the MSFC X-Ray Calibration Facility", *X-Ray and Extreme Ultraviolet Optics*, Proc. SPIE, Vol. **2515**, 420-435 (1995).
12. T.H. Markert, C.R. Canizares, D. Dewey, M. McGuirk, C. Pak, and M.L. Schattenburg, "The High Energy Transmission Grating Spectrometer for AXAF", *EUX, X-Ray, and Gamma-Ray Instrumentation for Astronomy V*, Proc. SPIE, Vol. **2280**, 168-180 (1994).
13. H.L. Marshall, D. Dewey, K.A. Flanagan, C. Baluta, C.R. Canizares, D.S. Davis, J.E. Davis, T.T. Fang, D.P. Huenemoerder, J.H. Kastner, N.S. Schulz, M.W. Wise, J.J. Drake, J.Z. Juda, M. Juda, A.C. Brinkman, C.J.Th. Gunsing, and J.S. Kaastra, G. Hartner and P. Predehl, "Towards the Calibration of the HETG LRF", *Grazing Incidence and Multilayer X-Ray Optical Systems*, Proc. SPIE, Vol. **3113**, 160-171 (1997).
14. N. S. Schulz, D. Dewey, and H. L. Marshall, "Absolute Effective Areas of the HETGS", Proc. SPIE, Vol. **?**, (1998).
15. M.D. Stage and D. Dewey, "Verifying the HETG Spectrometer Rowland Design", *X-Ray Optics, Instruments, and Missions*, Proc. SPIE, Vol. **3444**, (1998).
16. D.A. Swartz, R.F. Elsner, J.J. Kolodziejczak, S.L. O'Dell, A.F. Tennant, M.E. Sulkanen, M.C. Weisskopf, and R.J. Edgar, "Use of Monochromators for the Calibration of AXAF", *X-Ray Optics, Instruments, and Missions*, Proc. SPIE, Vol. **3444**, (1998).
17. AXAF Science Center, "AXAF Observatory Guide",Rev. 1.0,available at *http://asc.harvard.edu* (1997).
18. M. Weisskopf, R.F. Elsner, S.L. 0'Dell and the AXAF Project Science team, "Calibration of the Advanced X-ray Astrophysics Facility: Project Science analyses" available at *http://wwwastro.msfc.nasa.gov/xray/axafps.html* (1997).
19. M.C. Weisskopf and S.L. O'Dell, "Calibration of the AXAF observatory: overview", *Grazing Incidence and Multilayer X-Ray Optical Systems*, Proc. SPIE, Vol. **3113**, 2-17 (1997).
20. M.C. Weisskopf and S.L. O'Dell, "Calibration of AXAF: overview", *X-Ray Optics, Instruments, and Missions*, Proc. SPIE, Vol. **3444**, (1998).